

Hypernuclear stars from relativistic Hartree-Fock density functional theory

Jia Jie Li¹, Wen Hui Long², and Armen Sedrakian^{3,1}

¹ Institute for Theoretical Physics, J. W. Goethe University, D-60438 Frankfurt am Main, Germany

² School of Nuclear Science and Technology, Lanzhou University, Lanzhou 730000, China

³ Frankfurt Institute for Advanced Studies, D-60438 Frankfurt am Main, Germany

Received: date /Accepted: date

Abstract. The hypernuclear matter is studied within the relativistic Hartree-Fock theory employing several parametrizations of the hypernuclear density functional with density dependent couplings. The equations of state and compositions of hypernuclear matter are determined for each parametrization and compact stars are constructed by solving their structure equations in spherical symmetry. We quantify the softening effect of Fock terms on the equation of state, as well as discuss the impact of tensor interactions, which are absent in the Hartree theories. Starting from models of density functionals which are fixed in the nuclear sector to the nuclear phenomenology, we vary the couplings in the hyperonic sector around the central values which are fitted to the hyperonic potentials in nuclear matter. We use the SU(6) spin-flavor and SU(3) flavor symmetric quark models to relate the hyperonic couplings to the nucleonic ones. We find, consistent with previous Hartree studies, that for the SU(6) model the maximal masses of compact stars are below the two-solar mass limit. In the SU(3) model we find sufficiently massive compact stars with cores composed predominantly of Λ and Ξ hyperons and a low fraction of leptons (mostly electrons). The parameter space of the SU(3) model is identified where simultaneously hypernuclear compact stars obey the astrophysical limits on pulsar masses and the empirical hypernuclear potentials in nuclear matter are reproduced.

1 Introduction

Neutron stars - remnants of luminous stars that are born in core-collapse supernovas - serve as unique laboratories for the exploration of dense hadronic matter [1–6].

Observations of the mass and/or the radius of a neutron star can provide a stringent constraint on the equation of state (EoS) of dense matter. The data indicates that the masses of pulsars in neutron star binaries are tightly clustered around the canonical mass value $1.4 M_{\odot}$, as was initially established for the pulsar B1913+16 discovered in the Hulse-Taylor binary. More recently, higher neutron star masses were measured with high precision in binaries containing millisecond pulsars, specifically $1.667 \pm 0.021 M_{\odot}$ for PSR J1903+0327 [7], $1.93 \pm 0.02 M_{\odot}$ for PSR J1614-2230 [8, 9] and $2.01 \pm 0.04 M_{\odot}$ for PSR J0348+0432 [10]. The last two measurements provide observationally reliable lower bounds on the maximum mass of a neutron star and thus set astrophysical constraints on the EoS of dense matter.

The accuracy with which the neutron star radii can be measured is less precise. These are commonly extracted from the analysis of X-ray binaries, which depends on the measurements of their distances, the amount of intervening absorbing material, and their atmospheric compositions. The values of neutron star radii conjectured in the literature lie in the range $10 \leq R \leq 14$ km [11–15] with uncertainties in the range $\sim 30\%$ or greater. NASA's NICER experiment [16], which was recently launched, will allow measurements of neutron star radii to un-

precedented precision with better than 10 percent uncertainty. Finally, an alternative and independent information on neutron star radii can be obtained from the gravitational-wave (GW) signals emitted in neutron star mergers. The accuracy of a radius measurement in this case can be comparable to the best X-ray observations [17, 18].

The recent simultaneous detection of a GW signal by LIGO and Virgo [19] of neutron star binary merger event (GW170817 event) set bounds on the tidal deformabilities of compact stars [19]. This information, which is complimentary to the mass and radius measurements mentioned above, can be used to constraint further the EoS of ultra-dense matter [20, 21].

While medium mass stars may contain purely nucleonic matter in their centers, the stars close to the maximum mass reach central densities roughly by an order of magnitude larger than the saturation density. At such densities a number of new degrees of freedom such as hyperons, deltas, and deconfined quark matter, may be present. The formation of hyperons which is predicted by modern models of dense matter at densities of about $(2-3)\rho_0$, where ρ_0 is the nuclear saturation density, leads to sizeable softening of the EoS and, consequently, the maximum mass of neutron stars with hyperons decreases to values which are incompatible with the mass-measurements quoted above. This is known as the "hyperon puzzle" which is the main focus of this work.

The relativistic density functional theories (DFTs) [22–26] provide a convenient tool to address the problem of the equa-

tion of state (EoS) of dense matter and the structure of neutron stars, in particular the problem of hyperonization at high densities. Several version of the relativistic DFTs have been employed for this purpose so far: (a) DFs which incorporate nonlinear (NL) self-interaction of the mesons [27–35]; (b) DFs with density-dependent (DD) meson-baryon couplings [36–47]; (c) quark-meson coupling models [48–52].

In this work we provide a first treatment of the full baryon octet within the relativistic Hartree-Fock theory based on a DF with DD couplings, i.e., the class (b) models. To date the hyperonization of dense matter within the class (b) of DF models was addressed only at the level of the Hartree approximation [37–47], the only exception being the previous treatment which included the Λ hyperon [36]. In doing so, we adopt the strategy of using the SU(3) symmetric quark model for fixing the DD coupling constants of hyperons to the nucleonic ones, previously used in the Hartree theories, see e.g. [28, 29, 37–39], combined with constraints placed by the depth of the hyperonic potentials in nuclear matter.

Thus, we take the previous studies based on Hartree approximation to a new level of many body theory, which has a number of advantages: (a) the contributions of the Fock terms to the hyperonic self-energies are explicit; (b) the tensor interactions arising for example from pion exchanges, which are absent in the Hartree theories, are fully taken into account. (c) the space component of vector self-energy arising from Fock terms could be important beyond the saturation density; (d) the Fock contributions ensure the proper antisymmetrization of baryon wave function in matter. We take into account two constraints available to tune the hypernuclear interactions: (i) the depth of hyperonic potentials in nuclear matter are used as a guide to fix the range of hyperonic couplings; (ii) the measured masses of neutron stars are used to select the viable models.

In closing this section, we note that the case of non-strange nuclear matter within the framework adopted in this work has been extensively studied and gauged to reproduce the nuclear phenomenology [53–59]. In particular the role of the Fock terms and the tensor interactions in determining the nuclear structure properties has been discussed in Refs. [60–64]. The non-strange models produce heavy enough neutron stars with the maximum in the range $2.4 M_\odot$ [65], which guarantees that moderate softening due to introduction of hyperons can still produce large enough masses for hypernuclear compact stars.

This paper is organized as follows. In Sect. 2, we describe in some detail the formalism of DFT in relativistic Hartree-Fock (RHF) approximation and its extension to the baryon octet. In Sect. 3 we discuss the EoS of hypernuclear matter. Our numerical results are presented in Sect. 4. Section 5 contains our conclusions and the perspectives of this research. Some details of our calculations and the input physics are relegated to the Appendices.

2 Theoretical formalism

In this section we outline the theoretical framework of the present work, which is based on the covariant DFT for hypernuclear matter. The functional is generated by evaluating the baryon self-energies in the Hartree-Fock approximation. The

Table 1. The properties of baryon octet with a spin 1/2. The mass (in MeV), spin j , isospin τ and its third component τ_3 , charge q , and strangeness s .

Octet	Mass	j	τ	τ_3	q	s
n	939.57	1/2	1/2	-1/2	0	0
p	938.27			1/2	1	
Λ	1115.68	1/2	0	0	0	-1
Σ^-	1197.45	1/2	1	-1	-1	-1
Σ^0	1192.64			0	0	
Σ^+	1189.37			1	1	
Ξ^-	1321.71	1/2	1/2	-1/2	-1	-2
Ξ^0	1314.86			1/2	0	

Table 2. Quantum numbers and mass (in MeV) of mesons.

Meson	π	ρ	σ	ω	σ^*	ϕ
J^π	0^-	1^-	0^+	1^-	0^+	1^-
T	1	1	0	0	0	0
Mass	138	769	~ 500	783	975	1020

interaction part of the Lagrangian of hypernuclear matter contains the couplings between the baryons and mesons which, as usual, have to be fitted to the experimental (empirical) data. Table 1 lists the key properties of the spin-1/2 baryon octet considered in this work. The meson degrees of freedom included in our treatment are listed in Table 2 and are arranged according to their quantum number (J^π, T), where J is the spin, π is the intrinsic parity and T is the isospin. In addition to the usual set of meson acting in nuclear matter, we have added two additional hidden-strangeness mesons, σ^* and ϕ . Note that the mass of the σ meson, which is supposed to represent the two π -exchange contribution to the nuclear force, is not known with precision and lies around 500 MeV.

2.1 Computation of the self-energies

The Lagrangian of the hypernuclear matter is the sum of the free baryonic and mesonic Lagrangians, \mathcal{L}_B and \mathcal{L}_M and an interaction Lagrangian \mathcal{L}_{int} which describes the coupling between baryon fields via meson exchange

$$\mathcal{L} = \mathcal{L}_B + \mathcal{L}_M + \mathcal{L}_{\text{int}}. \quad (1)$$

The free baryonic Lagrangian is given by the sum of Dirac Lagrangians of individual baryons of mass M_B

$$\mathcal{L}_B = \sum_B \bar{\psi}_B (i\gamma_\mu \partial^\mu - M_B) \psi_B, \quad (2)$$

where index B sums over the baryonic octet. The mesonic Lagrangian has the form

$$\begin{aligned} \mathcal{L}_M = & + \frac{1}{2} \partial^\mu \sigma \partial_\mu \sigma - \frac{1}{2} m_\sigma^2 \sigma^2 + \frac{1}{2} \partial^\mu \sigma^* \partial_\mu \sigma^* - \frac{1}{2} m_{\sigma^*}^2 \sigma^{*2} \\ & - \frac{1}{4} \Omega^{\mu\nu} \Omega_{\mu\nu} + \frac{1}{2} m_\omega^2 \omega^\mu \omega_\mu - \frac{1}{4} \Phi^{\mu\nu} \Phi_{\mu\nu} + \frac{1}{2} m_\phi^2 \phi^\mu \phi_\mu \\ & - \frac{1}{4} R^{\mu\nu} R_{\mu\nu} + \frac{1}{2} m_\rho^2 \rho^\mu \rho_\mu + \frac{1}{2} \partial^\mu \pi \partial_\mu \pi - \frac{1}{2} m_\pi^2 \pi^2, \quad (3) \end{aligned}$$

with $\Omega^{\mu\nu}$, $\Phi^{\mu\nu}$ and $R^{\mu\nu}$ being the field strength tensors for the vector mesons. The interaction Lagrangian is given by

$$\begin{aligned} \mathcal{L}_{\text{int}} = & \sum_B \bar{\psi}_B \left(-g_{\sigma B} \sigma - g_{\sigma^* B} \sigma^* \right. \\ & - g_{\omega B} \gamma^\mu \omega_\mu - g_{\phi B} \gamma^\mu \phi_\mu - g_{\rho B} \gamma^\mu \rho_\mu \cdot \tau_B \\ & + \frac{f_{\omega B}}{2M_B} \sigma^{\mu\nu} \partial_\mu \omega_\nu + \frac{f_{\phi B}}{2M_B} \sigma^{\mu\nu} \partial_\mu \phi_\nu + \frac{f_{\rho B}}{2M_B} \sigma^{\mu\nu} \partial_\mu \rho_\nu \cdot \tau_B \\ & \left. - \frac{f_{\pi B}}{m_\pi} \gamma_5 \gamma^\mu \partial_\mu \pi \cdot \tau_B \right) \psi_B, \end{aligned} \quad (4)$$

where $\sigma^{\mu\nu} = \frac{i}{2} [\gamma^\mu, \gamma^\nu]$, τ_B is the vector of isospin Pauli matrices, with $\tau_{3,B}$ being its third component. The mesons couple to the baryons with the strengths determined by the coupling constants $g_{\alpha B}$ and $f_{\alpha B}$.

The full baryon propagator is defined through Dyson's equation

$$G(k) = G^0(k) + G^0(k) \Sigma(k) G(k), \quad (5)$$

where G^0 is the Green's function in free space, k is the four momentum of baryon, and Σ is the baryon self-energy. Because of the requirement of translational and rotational invariance in the rest frame of infinite matter, the most general form of the decomposition of the self-energy in the Dirac space is given by

$$\Sigma(k) = \Sigma_S(k) + \gamma_0 \Sigma_0(k) + \boldsymbol{\gamma} \cdot \hat{\mathbf{k}} \Sigma_V(k), \quad (6)$$

where $\hat{\mathbf{k}}$ is the unit vector along \mathbf{k} , with Σ_S , Σ_0 and Σ_V being the scalar, time and space components of the vector self-energies.

By introducing the following auxiliary quantities

$$\mathbf{k}^* = \mathbf{k} + \hat{\mathbf{k}} \Sigma_V, \quad (7a)$$

$$M^* = M + \Sigma_S, \quad (7b)$$

$$E^* = E - \Sigma_0, \quad (7c)$$

the Dirac equation in infinite matter can be written in a form resembling the free-space Dirac equation

$$(\boldsymbol{\gamma} \cdot \mathbf{k}^* + M^*) u(k, s, \tau) = \gamma^0 E^* u(k, s, \tau), \quad (8)$$

where $u(k, s, \tau)$ have the meaning of Dirac spinors. In addition we define the quantities \hat{P} and \hat{M}

$$\hat{P} \equiv \frac{\mathbf{k}^*}{E^*}, \quad \hat{M} \equiv \frac{M^*}{E^*}, \quad (9)$$

which we will use in the expressions of self-energies.

As well known, the ground state of *interacting* fermionic matter is obtained by filling energy levels with spin-isospin degeneracy γ up to the Fermi momentum k_F . A straightforward computation of the Hartree (i.e. direct interaction) contribution to the components of Lorentz decomposition (6) of the self-energy gives

$$\Sigma_{S,B}^H = -g_{\sigma B} \bar{\sigma} - g_{\sigma^* B} \bar{\sigma}^*, \quad (10a)$$

$$\Sigma_{0,B}^H = +g_{\omega B} \bar{\omega} + g_{\phi B} \bar{\phi} + g_{\rho B} \tau_{3,B} \bar{\rho}, \quad (10b)$$

$$\Sigma_{V,B}^H = 0. \quad (10c)$$

In the present calculation, we ignore the retardation effects which amount to rather small contributions (at most a few percent) to the self-energies [66]. The contributions of the Fock terms (corresponding to exchange interactions) are therefore given by

$$\begin{aligned} \Sigma_{S,B}^F(k, \tau) = & \frac{1}{(4\pi)^2 k} \sum_{\alpha, B'} \tau_\alpha^2 \int_0^{k_{F,B'}} k' dk' \left[\hat{M}(k') B_\alpha(k, k') \right. \\ & \left. + \frac{1}{2} \hat{P}(k') D_\alpha(k, k') \right], \end{aligned} \quad (11a)$$

$$\Sigma_{0,B}^F(k, \tau) = \frac{1}{(4\pi)^2 k} \sum_{\alpha, B'} \tau_\alpha^2 \int_0^{k_{F,B'}} k' dk' A_\alpha(k, k'), \quad (11b)$$

$$\begin{aligned} \Sigma_{V,B}^F(k, \tau) = & \frac{1}{(4\pi)^2 k} \sum_{\alpha, B'} \tau_\alpha^2 \int_0^{k_{F,B'}} k' dk' \left[\hat{P}(k') C_\alpha(k, k') \right. \\ & \left. + \frac{1}{2} \hat{M}(k') D_\alpha(k, k') \right], \end{aligned} \quad (11c)$$

where α sums over mesons, $k_{F,B}$ is the baryon Fermi momentum and τ_α is the isospin factor at the meson-baryon vertex in the Fock diagram. The explicit expression for the functions A_α , B_α , C_α and D_α in Eqs. (11) are given in Appendix A.

The meson fields obey in general inhomogeneous Klein-Gordon equations for scalar mesons and Proca equations for vector mesons. As well known, the current conservation implies that the Proca equations can be further reduced to Klein-Gordon equations. In the mean-field approximation, the meson fields are replaced by their respective mean-field expectation values,

$$\bar{\sigma} = \frac{1}{m_\sigma^2} \sum_B g_{\sigma B} \rho_{s,B}, \quad \bar{\sigma}^* = \frac{1}{m_{\sigma^*}^2} \sum_B g_{\sigma^* B} \rho_{s,B}, \quad (12a)$$

$$\bar{\omega} = \frac{1}{m_\omega^2} \sum_B g_{\omega B} \rho_{v,B}, \quad \bar{\phi} = \frac{1}{m_\phi^2} \sum_B g_{\phi B} \rho_{v,B}, \quad (12b)$$

$$\bar{\rho} = \frac{1}{m_\rho^2} \sum_B g_{\rho B} \tau_{3,B} \rho_{v,B}, \quad (12c)$$

where the scalar and vector densities are given by

$$\rho_{s,B} \equiv \langle \bar{\psi} \psi \rangle = \frac{1}{\pi^2} \int_0^{k_{F,B}} k^2 dk \hat{M}_B, \quad (13a)$$

$$\rho_{v,B} \equiv \langle \psi^\dagger \psi \rangle = \frac{1}{\pi^2} \int_0^{k_{F,B}} k^2 dk = \frac{1}{3\pi^2} k_{F,B}^3. \quad (13b)$$

In addition, in infinite nuclear matter the spatial gradients of the fields can be neglected.

Because of the density dependence of meson-baryon couplings, we need to take into account the rearrangement in the interaction, which amounts to additional Σ_R contribution to the self-energy component $\Sigma_0(k)$

$$\begin{aligned} \Sigma_R = & \sum_\alpha \frac{\partial g_{\alpha B}}{\partial \rho_B} \sum_B \frac{1}{\pi^2} \int k^2 dk \left[\hat{M}_B(k) \Sigma_{S,B}^\alpha(k) \right. \\ & \left. + \Sigma_{0,B}^\alpha(k) + \hat{P}_B(k) \Sigma_{V,B}^\alpha(k) \right]. \end{aligned} \quad (14)$$

Including rearrangement is mandatory to ensure thermodynamic consistency of our model. Note that the rearrangement does

not contribute to the energy density but modifies the pressure. Attempts have been made to include phenomenologically the effect of short-range correlations in the Hartree-Fock studies of nuclear matter and nuclei [67], which should mimic the effect that arises from the resummations of ladder diagrams in the non-perturbative approaches. We do not include any phenomenological corrections that should account for short-range correlations.

2.2 Thermodynamics relations

Once the Hartree-Fock self-energies are determined, the computation of the energy density and the pressure of hypernuclear matter at zero temperature is standard. One starts with the field-theoretical expression for the energy-momentum tensor $T^{\mu\nu}$ in the Lagrangian formalism

$$T^{\mu\nu} = \frac{\partial \mathcal{L}}{\partial(\partial_\mu \varphi_i)} \partial^\nu \varphi_i - \eta^{\mu\nu} \mathcal{L}, \quad (15)$$

where φ_i stands generically for a boson or fermion field. The energy density is given by

$$\mathcal{E} \equiv \langle T^{00} \rangle, \quad (16)$$

which includes sum over all baryons and mesons in the model and $\langle \dots \rangle$ refers to the statistical average. The energy density is then obtained as

$$\mathcal{E}_B = \frac{\gamma_B}{2\pi^2} \int_0^{k_{F,B}} k^2 dk [T_B(k) + \frac{1}{2} V_B(k)] \quad (17)$$

with

$$T_B(k) = \hat{P}_B k_B + \hat{M}_B M_B, \quad (18a)$$

$$V_B(k) = \hat{M}_B \Sigma_{S,B}(k) + \hat{P}_B \Sigma_{V,B}(k) - \Sigma_{0,B}(k). \quad (18b)$$

In a similar way, one finds the pressure as the statistical average of the trace of the spatial component T^{ij} of energy-momentum tensor

$$\mathcal{P} \equiv \frac{1}{3} \sum_i \langle T^{ii} \rangle. \quad (19)$$

Thermodynamic consistency implies that the same can be obtained from the thermodynamic relation,

$$\mathcal{P}_B = \rho_B^2 \frac{\partial \mathcal{E}_B}{\partial \rho_B}. \quad (20)$$

2.3 Stellar matter and structure

We now complete the discussion of thermodynamics of hypernuclear matter by pointing out the additional conditions of weak equilibrium and charge neutrality that prevail in neutron stars. These conditions imply that the stellar matter consists

of not only baryon octet but also leptons l ($l = e^-, \mu^-$). The Lagrangian density for noninteracting leptons is given by the standard Dirac Lagrangian and their energy density and pressure at zero temperature read

$$\mathcal{E}_l = \frac{1}{\pi^2} \int_0^{k_{F,l}} dk k^2 (k^2 + m_l^2)^{1/2}, \quad (21a)$$

$$\mathcal{P}_l = \frac{1}{3\pi^2} \int_0^{k_{F,l}} dk k^4 (k^2 + m_l^2)^{-1/2}, \quad (21b)$$

where $k_{F,l}$ is the lepton Fermi momentum, m_l is the lepton bare mass. The contribution of leptons should be added to the energy density and pressure of hadronic matter once the chemical potentials of the baryon-lepton mixture are determined, i.e.,

$$\mathcal{E}_H = \sum_B \mathcal{E}_B + \sum_l \mathcal{E}_l, \quad \mathcal{P}_H = \sum_B \mathcal{P}_B + \sum_l \mathcal{P}_l. \quad (22)$$

In β equilibrium the chemical potentials of the particles are related to each other by

$$\mu_B = b_B \mu_n - q_B \mu_e, \quad (23)$$

where b_B and q_B denote the baryon number and electric charge of baryon species B . This condition guarantees that all reactions which conserve charge and baryon number are allowed. Explicitly, the condition of β equilibrium is expressed as

$$\mu_n = \mu_\Lambda = \mu_{\Sigma^0} = \mu_{\Xi^0}, \quad (24a)$$

$$\mu_n + \mu_e = \mu_{\Sigma^-} = \mu_{\Xi^-}, \quad (24b)$$

$$\mu_n - \mu_e = \mu_p = \mu_{\Sigma^+}, \quad (24c)$$

$$\mu_e = \mu_\mu, \quad (24d)$$

where the chemical potentials for baryons and leptons are given by

$$\mu_B = \Sigma_0(k_{F,B}) + E^*(k_{F,B}), \quad (25a)$$

$$\mu_l = (k_{F,l}^2 + m_l^2)^{1/2}. \quad (25b)$$

In the expressions above, Σ_0 contains Hartree [Σ_0^H , Eq. (10)] and Fock [Σ_0^F , Eq. (11)] contributions as well as the rearrangement term Σ_R which is given by Eq. (14). Furthermore, charge neutrality is imposed as

$$\sum_B q_B \rho_B + \sum_l q_l \rho_l = 0. \quad (26)$$

The conservation laws imply that there are only two independent chemical potentials related to baryon number density and total charge density.

The above conditions, together with the field equations for baryons and mesons, allow one to determine the equilibrium composition ρ_B and ρ_l at a given baryon number density and determine the EoS of matter.

The spherically symmetric solutions of Einstein's equations for self-gravitating fluids are given by the Tolman-Oppenheimer-Volkoff (TOV) equations [68, 69]. In the geometrized units $c = G = 1$, the TOV equations read

$$\frac{dP(r)}{dr} = - \frac{[P(r) + \varepsilon(r)][M(r) + 4\pi r^3 P(r)]}{r[r - 2M(r)]}, \quad (27a)$$

$$\frac{dM(r)}{dr} = 4\pi r^2 \varepsilon(r), \quad (27b)$$

where $P(r)$ is the pressure of the star at radius r , and $M(r)$ is the total star mass inside a sphere of radius r . To construct equilibrium models of compact stars we supplement the EoS of infinite hypernuclear matter with the EoS of inhomogeneous low-density matter in the crusts at the transition density $\rho_0/2$. Specifically, for the inner and outer crust we use the EoS of Refs. [70] and [71]. It is worthwhile to mention that the crust-core matching procedure can affect the value of the radius of less massive stars [72]. However, in the present work, we concentrate mainly on the maximum-mass compact stars, for which the radius is not very sensitive to the matching procedures [72].

3 Equations of state

The wealth of nuclear data allows one to constrain the nucleon-nucleon (NN) interaction within reasonable accuracy, whereas this is not the case for hyperon-nucleon (YN) and hyperon-hyperon (YY) interactions, where data are scarce. We try to construct an effective NY or YY interaction for use in the many-body environment, starting from a nucleonic RHF density functional (hereafter DF) which quantitatively fits the nuclear data.

3.1 Meson-nucleon couplings

In this work we will use density-dependent meson-baryon couplings, which are designed to account in an economical manner for the many-body corrections that arise beyond the mean-field approximation. Such density dependencies of the coupling constants are designed to account for the influence of the medium on the scattering amplitude of baryons, as explicitly accounted for in the DBHF theories of nuclear matter. Below we consider four parametrizations designed for RHF computations, namely PKO1-3 [53, 60] and PKA1 [54], as well as two standard parametrizations of RH DF, specifically DD-ME2 [78] and GM1 [79]. Some details of the RHF parametrizations for nuclear matter characteristics are compared in Table 3. Note also that the RH-GM1 DF is fitted only to the properties of bulk nuclear matter.

In Fig. 1 (a) we show the energy per nucleon for pure neutron matter at and below the saturation density. The band represents the results based on chiral effective field theory (ChEFT), which includes an estimate of the uncertainties related to the three-body force [73]. In the relevant density region $0.5 \leq \rho_B/\rho_0 \leq 1.2$, i.e., the region where one deals with homogeneous neutron matter in neutron stars, the DFs PKO2 and PKO3 are fully consistent with the results of ChEFT. The DFs PKA1 and PKO1 overshoot the ChEFT band by several MeV at close to saturation density. Among the RH DFs the DD-ME2 is seen to be consistent with the ChEFT results, whereas the remaining DFs show considerable deviation in the low-density (GM1, IUFSU) and close-to-saturation (TM1) regime.

The symmetry energy and its derivatives are important characteristics of any model of nuclear EoS. Intensive efforts, both theoretical and experimental, have been made to constrain symmetry energy and its density dependence. Figure 1(b) shows the symmetry energy as a function of baryon density for the models discussed above. We present also the data from simulations

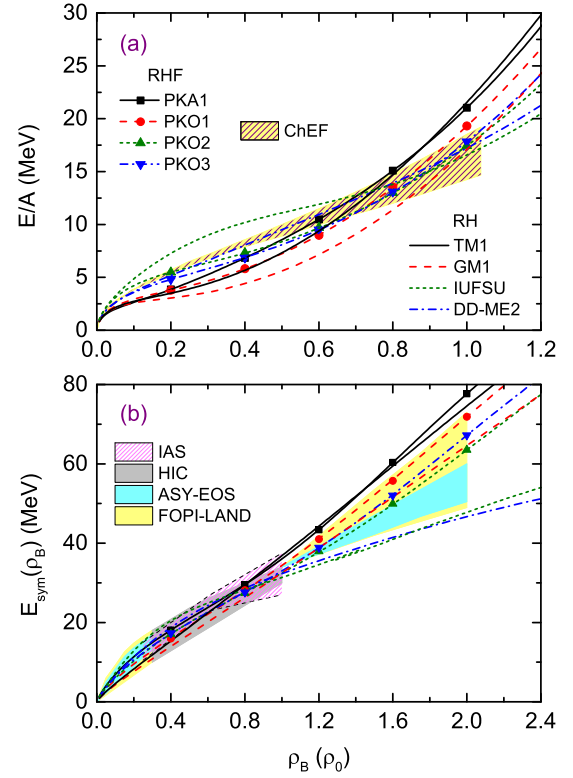


Fig. 1. (a) The energy per nucleon in pure neutron matter as functions of baryon density within different DFs compared with the chiral effective field (ChEF) theory of Ref. [73]. (b) The symmetry energy as a function of baryon density. The shaded regions represent the experimental constraints deduced from HIC (Sn+Sn) [74], FOPI-LAND [75], ASY-EOS [76] and IAS [77].

of heavy ion collisions [74–76] and nuclear structure studies, which are based on excitation to isobaric analog states [77]. As can be seen, the symmetry energy at low densities ($\rho_B \leq \rho_0$) predicted by our collection of models is consistent with the experimental data. However, sizeable deviations are seen for densities beyond the saturation density. In particular, the symmetry energy of the RHF DFs above saturation is higher than the one suggested by the ASY-EOS experiment [76] and the one predicted by PKA1 DF lies above the band of FOPI-LAND experiment [75].

Figure 2(a) summarizes the symmetry energy at the saturation density J versus its slope L for RHF DFs used in this work along with some other frequently used RH DFs. The collection of shown DFs include the DD-RHF parametrizations PKO1-3 [53, 60], PKA1 [54], the DD-RH parametrizations include TW99 [80], DD1 [81], DD2 [82], DDF [83], PKDD [84], DD-ME1 [85], DD-ME2 [78], DD-ME δ [86], and the NL-RH parametrizations GM1, GM3 [79], TM1 [87], TMA [88], NL3 [89], NL3* [90], PK1, PK1r [84], FSU [91], FSU2 [92], IU-FSU [93], SFHo, SFHx [94]. Extensive, independent studies have been performed to constrain the values of these quantities, but the uncertainties are still large especially for the slope L . In this figure, the soft EoSs are located at the lower left corner where the values of J and L are small, whereas the hard EoSs are located at the upper right corner where the values of these parameters are large. It is clearly seen that the softest ones are those

Table 3. Bulk properties of symmetric nuclear matter at the saturation point: density ρ_0 (fm^{-3}), binding energy E_B (MeV), compression modulus K (MeV), symmetry energy J (MeV) and its slope L (MeV), Dirac mass M_D^* (M), where M is the bare mass, and nonrelativistic effective mass M_{NR}^* (M) predicted by selected RHF and RH DFs. The nonrelativistic effective masses of neutrons $M_{NR}^*(n)$ and protons $M_{NR}^*(p)$ in neutron matter are also listed.

DF	Interaction	Symmetric matter						Neutron matter		
		ρ_0	E_B	K	J	L	M_D^*	M_{NR}^*	$M_{NR}^*(n)$	$M_{NR}^*(p)$
RHF	PKA1	0.160	-15.83	229.96	36.02	103.50	0.55	0.68	0.68	0.70
	PKO1	0.152	-16.00	250.28	34.37	97.71	0.59	0.75	0.73	0.76
	PKO2	0.151	-16.03	249.53	32.49	75.92	0.60	0.76	0.75	0.77
	PKO3	0.153	-16.04	262.44	32.99	82.99	0.59	0.74	0.74	0.76
RH	DD-ME2	0.152	-16.14	251.15	32.31	51.27	0.57	0.65	0.64	0.70
	GMI	0.153	-16.33	300.22	32.51	93.96	0.70	0.77	0.73	0.81

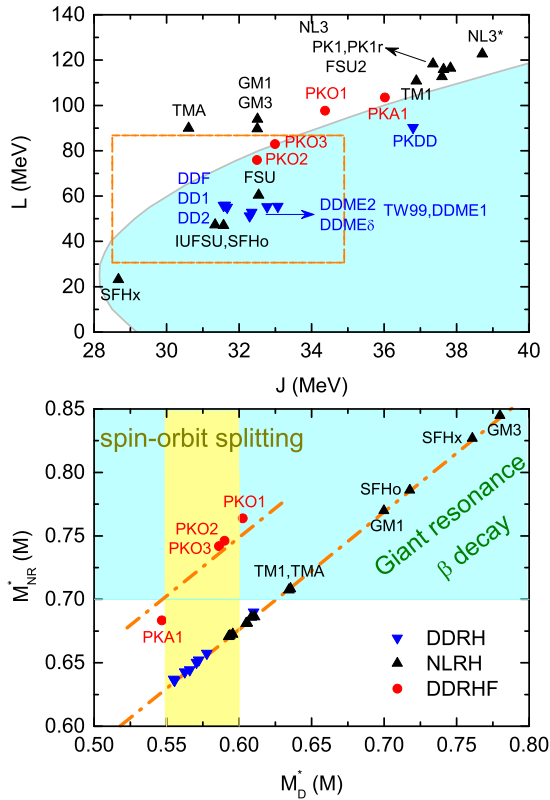


Fig. 2. (a) The location of different relativistic nuclear DFs in the plane spanned by the symmetry energy J and its slope L . The rectangle shows the bounds on the most probable values of symmetry energy $J = 31.7 \pm 3.2$ MeV and the slope $L = 58.7 \pm 28.1$ MeV obtained from the combined analysis of astrophysical constraints and terrestrial experiments [6]. The shaded region is the one allowed by the unitary gas bounds [95]. (b) The nonrelativistic effective masses M_{NR}^* versus Dirac masses M_D^* predicted by the DFs defined in panel (a). The dashed lines are shown to guide the eye. The realistic description of the spin-orbit splitting requires $M_D^* \in [0.55, 0.60]$ [81], and the giant resonances require $M_{NR}^* \in [0.70, 0.90]$ [96–99].

based on the DD-RH DFs, which are followed by moderately soft DD-RHF DFs, then by the hard non-linear RH DFs.

The effective mass, which characterizes the quasiparticle properties in a strongly interacting medium, is another important characteristic of a model; one distinguishes the Dirac mass,

Table 4. Astrophysical characteristics of the nucleonic EoS models: maximum mass M_{\max} (M_\odot), the corresponding central densities ρ_c (fm^{-3}) and radii R_{\max} (km), the radii $R_{1.4}$ (km) for the canonical mass $1.4M_\odot$ neutron stars, the density ρ_{DU} (fm^{-3}) and mass M_{DU} (M_\odot) threshold for the onset of direct Urca process (no entry means that the process is forbidden), calculated using RHF and RH DFs.

DF	M_{\max}	R_{\max}	ρ_c	$R_{1.4}$	ρ_{DU}	M_{DU}
PKA1	2.42	12.34	0.810	13.99	0.252	0.99
PKO1	2.44	12.41	0.801	14.13	0.251	1.01
PKO2	2.45	12.30	0.804	13.79	0.294	1.25
PKO3	2.49	12.49	0.780	13.96	0.282	1.23
DD-ME2	2.48	12.07	0.817	13.22	-	-
GMI	2.36	11.97	0.862	13.81	0.278	1.10

which is a genuine relativistic quantity without a nonrelativistic counterpart and the nonrelativistic mass defined in the context of Fermi-liquid theories [100]. Figure 2(b) shows the Dirac mass M_D^* and the nonrelativistic effective mass M_{NR}^* for a number of DFs. The realistic description of the spin-orbit splitting in finite nuclei places the constraint $0.55 \leq M_D^* \leq 0.60$ on the Dirac mass [81]. The excitation energies of quadrupole giant resonances in nuclei have shown that a realistic choice for the non-relativistic effective mass should be in the range $0.7 \leq M_{NR}^* \leq 0.90$ [96–99].

To complete the survey of models with non-strange baryons, we list in Table 4 the maximal mass of spherically-symmetrical, non-rotating and non-magnetized configuration supported by each model, its radius and central density. The maximum masses quoted are compatible with the current lower bound on the maximum mass of a neutron star. Clearly, the values of maximal masses leave some room for softening of the EoS through the onset of hyperons, which will be discussed later on. Table 4 also lists the radii predicted by the models for a star with the canonical mass $1.4 M_\odot$; these lie close to the upper range of radii inferred from the analysis of X-ray data [12, 14, 15]. Finally, the density and mass threshold for the onset of direct Urca (DU) process in purely nucleonic matter are shown. For RHF DFs the DU threshold is quite low, which means that the stars will cool rapidly by this process if nucleonic pairing does not slow down the cooling rate significantly.

3.2 Including strange mesons: ϕ - B and σ^* - B couplings

The baryonic interactions involving strangeness will be treated below within either the SU(6) or SU(3) symmetric quark models [101–103], see Appendix C. In the SU(6) symmetric model the ϕ meson has a vanishing ϕ - N coupling, whereas it does couple to nucleon in SU(3) symmetric model through the relation (44) of Appendix C. As commonly assumed, in what follows we will take $\tan \theta = 1/\sqrt{2}$, corresponding to ideal mixing; then one has

$$\frac{g_{\phi N}}{g_{\omega N}} = -\frac{\sqrt{3} + \sqrt{2}z(1-4\alpha_v)}{\sqrt{6} - z(1-4\alpha_v)}. \quad (28)$$

However, we need to insure that this new coupling in the SU(3) model does not spoil the fits to the purely nuclear data. To do so, we can make, consistent with Fierz transformation [104, 105], the replacement

$$\frac{\tilde{g}_{\omega N}^2}{m_\omega^2} = \frac{g_{\omega N}^2}{m_\omega^2} + \frac{g_{\phi N}^2}{m_\phi^2}, \quad (29)$$

where the $\tilde{g}_{\omega N}$ denotes the coupling for the case of $g_{\phi N} = 0$.

In Fig. 3 we show the EoSs of symmetric nuclear matter and pure neutron matter calculated using RHF DF with PKO3 parameterization for two typical cases in the SU(3) model, $z = 0, \alpha_v = 1$ and $z = 1/\sqrt{6}, \alpha_v = 0$, where the ϕ mesons plays an important role. It is clear seen that the EoSs of pure nuclear matter is almost independent of the variations in α_v and z . Similarly, one could introduce σ^* -meson within the SU(3) symmetric model without destroying the properties of nuclear matter. In this work, we assume that the σ^* meson does not couple to nucleons ($g_{\sigma^* N} = 0$). In other words, we shall use σ and σ^* mesons to constrain the nucleon-hyperon (NY) and hyperon-hyperon (YY) interactions, respectively. A non-zero $g_{\sigma^* N}$ will lead to a global readjustment of $g_{\sigma N}$ and $g_{\sigma^* Y}$, without any new information introduced.

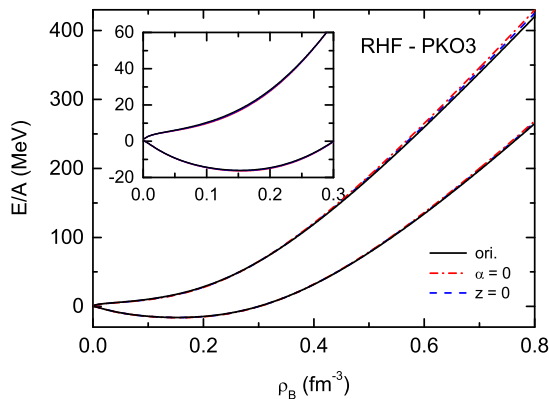


Fig. 3. Dependence of binding energies per nucleon in symmetric nuclear and pure neutron matter (lower and upper curves, respectively) on the baryonic density. The results are calculated with RHF theory with the original PKO3 parameterization as well as its modifications within the SU(3) symmetric model. The parameters of this model are chosen as $z = 0, \alpha_v = 1$ and $z = 1/\sqrt{6}, \alpha_v = 0$ which correspond to the cases where the ϕ mesons plays an important role. The inset shows the low-density region on a smaller scale.

3.3 Meson-hyperon couplings

The available experimental information on nucleon-hyperon (NY) and hyperon-hyperon (YY) interactions is scarce. Hyper-nuclei provide experimental information on the depths of hyperonic potential-wells in symmetric nuclear matter at saturation density. Additional information is obtained from nuclear reactions involving strangeness. Specifically, the reactions producing Λ -hypernuclei in the (π^+, K^+) associated production reactions [106, 107] and (K^-, π^-) strangeness exchange reactions, show that the ΛN interaction is definitely attractive. The binding energies of light to heavy Λ -hypernuclei are well reproduced by mean-field models [38, 47, 108–113]. The presently accepted value of the potential of the Λ particle in nuclear matter is $U_\Lambda^{(N)}(\rho_0) \approx -30 \text{ MeV}$. The information for ΞN interaction is more uncertain, the few current experimental data indicating that the corresponding potential depth $U_\Xi^{(N)}(\rho_0)$ is negative too, i.e., the interaction is attractive. The analysis of the missing-mass spectra of production reactions $^{12}\text{C} (K^-, K^+) \Xi^{\pm}\text{Be}$ suggests that the attractive potential for Ξ is smaller, $U_\Xi^{(N)}(\rho_0) \approx -14 \text{ MeV}$ [114]. Finally, the situation with the ΣN interactions is ambiguous. The analysis of (π^-, K^+) reactions on medium to heavy nuclei revealed a repulsive potential of the order of 40 MeV or less [115, 116], while the observation of a $^4_\Sigma\text{He}$ bound state in the $^4\text{He}(K^-, \pi^-)$ reaction seems to be in favor of an attractive potential [117]. Furthermore, the fits of Σ -atomic data indicate a transition from an attractive Σ potential at the surface to a repulsive one in the interior of a nucleus [118]. Therefore, we shall adopt below a repulsive potential for Σ hyperon in nuclear matter $U_\Sigma^{(N)}(\rho_0) \approx 30 \text{ MeV}$.

Motivated by the above considerations, we determine the coupling constants, $g_{\sigma Y}$, using the following values of hyperon potentials in symmetric nuclear matter at saturation:

$$U_\Lambda^{(N)}(\rho_0) = -30 \text{ MeV}, \\ U_\Xi^{(N)}(\rho_0) = -14 \text{ MeV}, \quad U_\Sigma^{(N)}(\rho_0) = 30 \text{ MeV}. \quad (30)$$

Note that the above potentials need to be considered as isoscalar hyperon potentials.

Using the baryon self-energies given in Eqs. (10) and (11), the potential for a single hyperon Y embedded in the nucleonic matter can be written as

$$U_Y^{(N)}(\mathbf{k}) = \Sigma_{S,Y}(\mathbf{k}) + \Sigma_{0,Y}(\mathbf{k}). \quad (31)$$

In the RHF theory, the self-energies are momentum dependent, therefore we consider their value at $\mathbf{k} = 0$, which corresponds to zero-momentum hyperon. Furthermore, the contribution of isovector mesons is small, even in symmetric nuclear matter, therefore we consider only the σ -scalar and $\omega(\phi)$ -vector couplings in the above expression. Note that rearrangement terms enter Eq. (31) via the $\Sigma_{0,Y}$ terms.

The existing few data on multi-hyperon nuclei comes from the measurements on light double- Λ nuclei. This provides the means of extracting the $\Lambda\Lambda$ interaction between Λ hyperons from the binding energy difference between double- Λ and single- Λ hypernuclei. However, the measured bond energies are subject to large uncertainty. The data on $^{10}_{\Lambda\Lambda}\text{Be}$ and $^{13}_{\Lambda\Lambda}\text{B}$ suggests that this energy is $\Delta B_{\Lambda\Lambda} \approx 5 \text{ MeV}$ [119, 120]. The data on $^6_{\Lambda\Lambda}\text{He}$

suggests a lower value $\Delta B_{\Lambda\Lambda} \approx 0.67 \pm 0.17$ MeV [121, 122]. Physically, one can interpret the bond energy as a rough estimate of the $U_{\Lambda}^{(\Lambda)}$ potential at the average Λ density ($\approx \rho_0/5$) inside the hypernucleus [113]. We adopt, therefore, the value

$$U_{\Lambda}^{(\Lambda)}(\rho_0/5) = -0.67 \text{ MeV}, \quad (32)$$

which reproduces the most accurate experimental data to date corresponding to the Nagara event [121, 122]. Note that this value represents the potential well of a zero-momentum of Λ particle in Λ matter. This information we use to fix the value of the coupling $g_{\sigma^*\Lambda}$. However, we would like to note that the value given by Eq. (32) is suggestive and is somewhat lower than the one obtained from the studies of ${}^6_{\Lambda\Lambda}\text{He}$ nucleus [47]. This study uses various RH DFs and calibrates the DF parameters to obtain the bond energy quoted above. From this procedure it find that $-3 \leq U_{\Lambda}^{(\Lambda)}(\rho_0/5) \leq -8$ MeV [47]. Also, the non-relativistic DF studies have shown that one could obtain precise bond energy by optimizing the ratio of the average Λ density to the saturation density in He [123, 124]. Note, however, that the extrapolation of information derived from few-body physics to statistical systems with large number of particles (here the infinite hypernuclear matter) is associated with large uncertainties, which translate into uncertainties in the couplings among hyperons.

The coupling of remaining hyperons Ξ and Σ to the σ^* is constrained by the relations

$$\frac{g_{\sigma^*Y}}{g_{\phi Y}} = \frac{g_{\sigma^*\Lambda}}{g_{\phi\Lambda}}, \quad Y \in (\Xi, \Sigma), \quad (33)$$

where ϕ refers to the ϕ -meson.

4 Numerical results and discussions

We now study the hyperonic matter within the RHF theory using several parametrizations of the meson-baryon couplings implied by the SU(6) and SU(3) flavor symmetric quark models and empirical hypernuclear data. The baryon-exchange and baryon-transition processes are beyond the scope of the present work and are disregarded below. We will use instead of $g_{\alpha Y}$ the ratio $R_{\alpha Y} = g_{\alpha Y}/g_{\alpha N}$. The density dependence of the meson-hyperon couplings is the same as the meson-nucleon ones.

The parametrizations PKO1-3 and PKA1 have been carefully tuned in the nuclear sector, therefore we prefer not to modify the parameters of these CDFs. At the same time, as a guide, we will use the SU(3)/SU(6) quark model relations in the hyperonic sector in order to reduce the number of the unknown coupling constants. By this, we do not imply a consistent SU(3)/SU(6) treatment of the full baryonic octet, since as mentioned above the nuclear sector remains fixed throughout our computation. Consequently, the true parameters are the ratios of the hyperonic to nucleonic couplings and not the parameters of the SU(3)/SU(6) model.

4.1 Stellar matter within the SU(6) symmetry

We start our discussion with the case where the coupling constants of vector meson-hyperon interactions are fixed by the

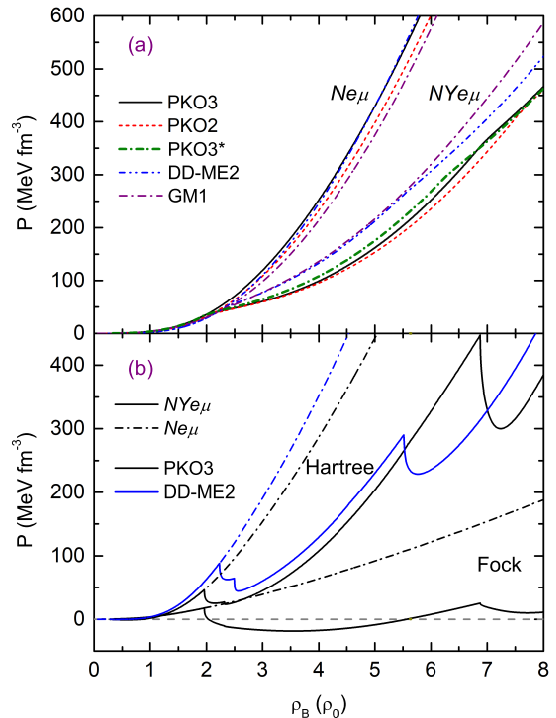


Fig. 4. (a) Dependence of the pressure of stellar matter with purely nucleonic and hyperonic compositions (labeled $Ne\mu$ and $NYe\mu$, with e, μ indicating electron and muon) on the normalized baryonic density. Calculations shown include the RHF parametrizations PKO2, PKO3 and the RH parametrizations DD-ME2, GM1 which have similar symmetry energy at the saturation point. The PKO3* result represents the EoS where the π -Y and the vector meson-Y tensor couplings are neglected. (b) Decomposition of the pressure resulting from the potential part of the interaction into Hartree and Fock channels. The results are shown in the cases of PKO3 and DD-ME2 parametrizations. The vector meson-hyperon coupling constants are fixed according to the SU(6) symmetric model.

SU(6) symmetric model, see Table 9 of 5. Although not entirely realistic, this model is instructive because it allows us to study the effects of the Fock terms, including the Lorentz tensor couplings associated with terms $\propto \sigma^{\mu\nu}$ in Eq. (4), on the EoS for neutron star matter.

4.1.1 Hartree approximation vs Hartree-Fock approximation

Our detailed numerical results were obtained using four parametrizations. Two of these are based on the RHF DFT and correspond to the PKO2 and PKO3 parametrizations; another two are based on more commonly used RH DFT, specifically on DD-ME2 and GM1 parametrizations. All these DFs predict similar EoS for purely nucleonic (i.e. $Ne\mu$) matter, see Fig. 4(a). As expected, the appearance of hyperons ($NYe\mu$) softens the EoS, which is reflected in the sudden change in the slope of the pressure at baryon density $\rho_B \approx 2.5\rho_0$, which corresponds to the threshold of the hyperon production. It is seen that quite generally the hyperonic EoSs based on RHF DFs are softer than those based on the RH DFs, as the Fock terms contribute with an opposite sign to the self-energy of fermions in general.

To elucidate this argument we show the separate contributions from the Hartree and Fock channels to the pressure in $Ne\mu$ matter and $NYe\mu$ matter in Fig. 4(b). For both compositions the pressures are dominated by the Hartree channels. In $Ne\mu$ matter both the Hartree and Fock contributions are smoothly increasing functions of the baryonic density, whereas in $NYe\mu$ matter these are discontinuous at the onset of hyperons. At the onset of hyperons the slope of the pressure of the Hartree and Fock contributions changes in a manner corresponding to a less repulsive interaction. We find that the Fock contribution at intermediate densities is decreasing and can become negative. One may thus conclude that the softening on the EoS in the RHF DFs is largely due to a pressure reduction induced by the Fock contribution.

The tensor interactions, originate from the π - and $\rho(\omega)$ -meson exchanges are clearly important in the NN -scattering and binding of deuteron. Since in the RH DFT the Fock diagrams are simply dropped, the RHF DFT becomes the only relativistic model which generates a tensor force. To show explicitly the impact of the tensor interactions on the EoS of dense matter we show in Fig. 4(a) a representative EoS PKO3* in which the π - Y and vector meson- Y tensor couplings are excluded. It is seen that within the SU(6) symmetric parameterization the inclusion of the tensor couplings tends to soften the EoS. Note that the tensor effects are mainly due to the isoscalar-vector mesons, since $\omega(\phi)$ - Y tensor couplings are much larger than $\rho(\pi)$ - Y ones. Furthermore, in the present models, the isovector meson couplings depend exponentially on density, therefore, the isovector fields are largely suppressed at high densities important for neutron stars.

The chemical equilibrium conditions listed in Eq. (24) determine the onset of hyperons, according to the criterion that hyperons appear in dense stellar matter when the maximal energy of the neutrons (Fermi energy) becomes comparable to the rest mass difference between hyperons and nucleons. In Fig. 5 we show the chemical potentials for neutral, positively charged, and negatively charged baryons in β equilibrium, as well as the points where the onset of hyperons occur. It is seen that the types of hyperons that are being populated are the same for the four selected parameterizations. The neutral baryon Λ appears first due to its small rest mass and larger attractive potential, with all the models predicting similar threshold densities ($2\rho_0$). In particular, the chemical potentials in RHF DFT with PKO2 and PKO3 parameterizations are lower than that those in RH DFT with DD-ME2 and GM1 parameterizations above the threshold density of Λ hyperon.

In $Ne\mu$ matter, the values of symmetry energy J and its slope L directly affect the chemical equilibrium of matter, in particular the neutron chemical potential. In general, for larger values of J the neutron chemical potential μ_n increases more rapidly with the density. As a result, μ_n , that defines the chemical potential of charge neutral baryons (e.g., Λ) is larger for models with large J . A larger value of L implies that the proton and electron chemical potentials (and their fractions) increase faster with the density. Because the sum $\mu_n + \mu_e$ defines the chemical potential of negatively charged baryons (e.g., Ξ^-), their onset densities is lower for larger values of L .

These arguments are useful for understanding the onset densities of Λ and Ξ^- hyperons in $NYe\mu$ matter. Indeed, to give

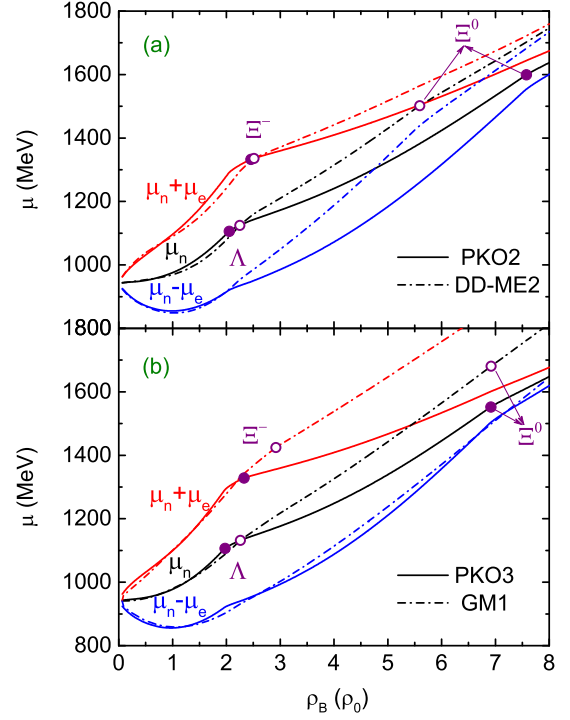


Fig. 5. Chemical potential for neutral, positively charged, and negatively charged baryons in β equilibrium, as a function of the normalized baryonic density. The results are calculated in the RHF-PKO2 (PKO3) DFs and are compared to the RH-DD-ME2 (GM1) DFs. The onsets of hyperons in the RHF DFs are shown by filled circles, in RH DFs by open ones. The vector meson-hyperon coupling constants are fixed according to SU(6) symmetric model.

a concrete example, we compare the RHF-PKO2 (PKO3) and RH-DD-ME2 DFs which differ mainly in the value of L . As seen from Fig. 5(a), below the threshold density of Λ , the neutron chemical potential for RHF-PKO2 DF (stiff symmetry energy) is slightly larger than the one of RH-DD-ME2 DF (soft symmetry energy), which leads to a smaller Λ onset density. However, the situation is reversed for the DFs PKO3 and GM1, used in Fig. 5(b), because in addition to the factors mentioned above isoscalar parameters of the DFs, such as the incompressibility K and Dirac mass M_D^* play a role.

It is also seen in these figures that as soon as hyperons appear, there are large differences between the values of the chemical potentials of the RHF and RH DFs. It is not easy to understand these differences in terms of the characters of the purely nucleonic matter. As seen from Fig. 5, in general, the density-dependence of the chemical potentials for RHF DFs are weaker than in RH DFs. We can speculate that the reason lies in the fact that Fock terms contribute to the chemical potentials with a sign which is opposite to the Hartree ones.

In this subsection, we illustrated the important features introduced by the Fock terms: they make the hyperonic EoS rather soft with their contribution to the pressure of matter becoming even negative. In the following, we shall restrict our attention to the RHF DFs.

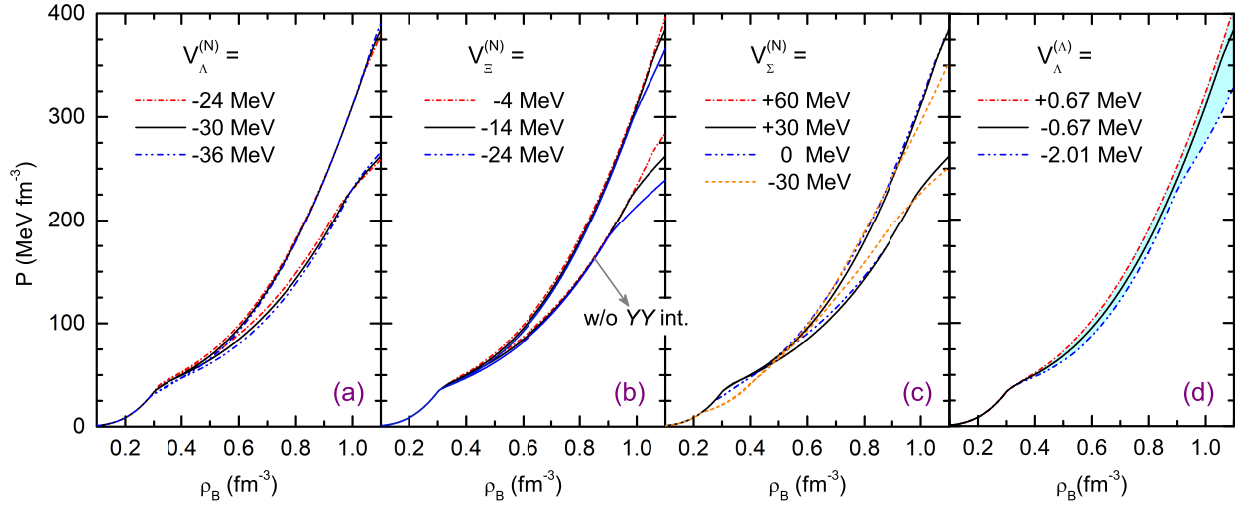


Fig. 6. Equations of state of hypernuclear matter for different values of isoscalar hypernuclear potentials in nuclear matter $V_Y^{(N)}(\rho_0)$ (panels a to c) and hypernuclear potentials in hypernuclear matter $V_\Lambda^{(A)}(\rho_0/5)$ (panel d). We tune the coupling constants $\sigma(\sigma^*)$ - Y while the others are fixed assuming SU(6) symmetry. (a) $V_Y \equiv (V_\Lambda^{(N)}, V_\Xi^{(N)}, V_\Sigma^{(N)}, V_\Lambda^{(A)}) = (-30 \pm 6, -14, +30, -0.67)$ MeV, the ordering of the EoSs according to their stiffness depends on the density interval; (b) $V_Y = (-24, -14 \pm 10, +30, -0.67)$ MeV; (c) $V_Y = (-30, -4, +30 \pm 30, -0.67)$ MeV, and in addition the case where $V_\Sigma^{(N)} = -30$ MeV; the EoSs are not much altered for positive $V_\Sigma^{(N)}$; (d) $V_Y = (-30, -14, +30, -0.67 \pm 1.34)$ MeV. The lower set of lines in panels (a-c) shows the results in the case where YY interactions are neglected. These results were calculated using the RHF DF with PKO3 parameterization.

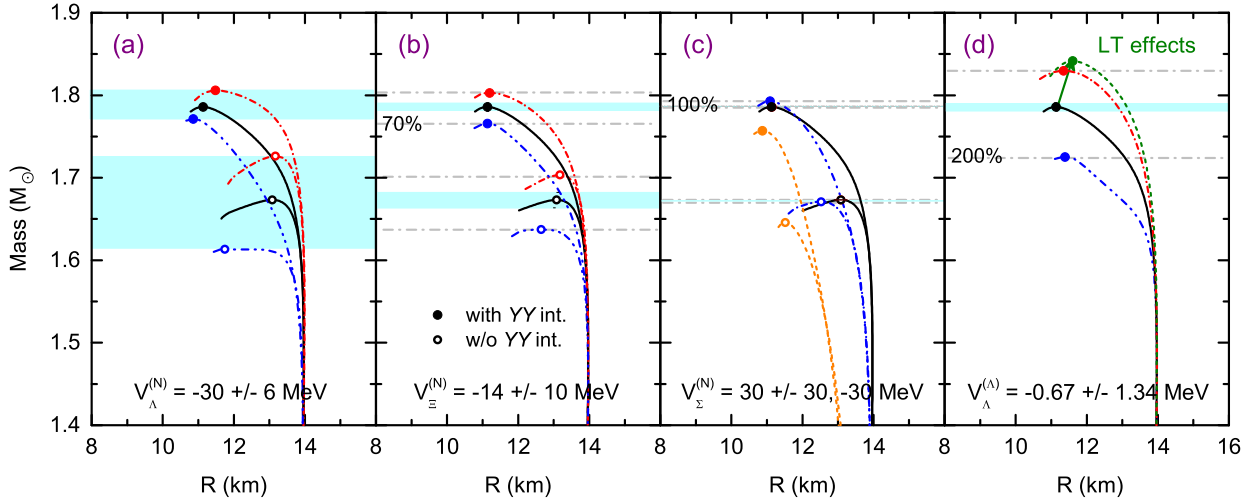


Fig. 7. Mass-radius relations for neutron stars for different values of isoscalar hypernuclear potentials. The circles show the point at which a neutron star reaches the maximum mass. The notations are the same as in Fig. 6. The shaded bands indicate the influences of varying V_Y by 20%, and those horizontal lines denote the influences of larger variations: for $V_\Xi^{(N)}$ by 70% (b), for $V_\Sigma^{(N)}$ by 100% (c), for $V_\Lambda^{(A)}$ by 200% (d). The effects of Lorentz tensor (LT) couplings are also indicated in panel (d).

4.1.2 Varying hyperon potentials

We now discuss the uncertainty in the hyperon potentials in nucleonic and hypernuclear matter. The potential depth for Λ has been determined more reliably than those for Ξ and Σ . Our strategy will be to keep fixed all hypernuclear potentials but one and vary the latter in a certain reasonable range by readjusting the $\sigma(\sigma^*)$ - Y coupling of the model. In Fig. 6, we show the EoSs of hypernuclear matter for different values of isoscalar hypernuclear potentials $V_Y^{(N)}(\rho_0)$ in nuclear matter [panels (a-c)] and the value of hypernuclear $V_\Lambda^{(A)}(\rho_0/5)$ potential in hypernuclear

matter [panel (d)]. The corresponding mass-radius relations of the compact star models derived from these EoSs are shown in Fig. 7. In both figures we also show the results where the YY interactions are omitted, i.e., σ^* - Y and ϕ - Y couplings are set to zero. It is clearly seen that the inclusion of strange σ^* and ϕ mesons has an overall repulsive effect and stiffens the EoS. It also suppresses the influence of uncertainty of hyperon potentials on the EoS.

We start our discussion with the potential depth of Λ by changing its value in the range $-36 \leq V_\Lambda^{(N)} \leq -24$ MeV which corresponds to 20% variations around its accepted value -30

MeV. We do this by readjusting the couplings $g_{\sigma\Lambda}$ and keeping all other potential depth fixed at values given in Eqs. (30) and (32). In the case where YY interactions are included there is no sizeable change in the EoS of hypernuclear matter and only slight variations when YY interactions are set to zero. The variations in the maximum mass of corresponding compact stars are in the range of $0.05 M_\odot$ in the first case and $0.1 M_\odot$ in the second case and the variations in the radii are of the order of 0.5 km.

In the case of Ξ potential we vary it in the range $-24 \leq V_\Xi^{(N)} \leq -4$ MeV around its accepted value -14 MeV. This corresponds to a variation of 70% around the central value. (The 20% variation in the magnitude of this potential has no effect on the EoS and stellar mass, see panel (b) of Fig. 7.) This leads to small variations in the EoS, which are reflected in the uncertainty band in the panel (b) of Fig. 7 of the order of $0.07 M_\odot$ in the maximum mass.

In the case of Σ hyperons, changing Σ potential $V_\Sigma^{(N)}(\rho_0)$ by 20% from the experimentally motivated value 30 MeV, we find no changes at all. In this case the Σ s are not present up to density $\rho_B = 8\rho_0$. Next we consider variations of this potential in the range $0 \leq V_\Sigma^{(N)} \leq 60$ MeV (which correspond to variation of 100% around the central value 30 MeV). We find that the EoS and the mass-radius relation are only slightly altered in this case. In addition we find that a weak repulsive potential, for example $V_\Sigma^{(N)}(\rho_0) \sim 5$ MeV, implies that Σ^- appears at lower density than the lightest hyperon Λ . This is a straightforward consequence of the conditions (24a) and (24b) according to which introducing Σ^- and removing an electron becomes energetically more favorable than adding a Λ particle. In addition, we study the effect of strongly attractive potential value $V_\Sigma^{(N)} = -30$ MeV. A strong attractive $V_\Sigma^{(N)}(\rho_0)$ leads to strong modifications of the EoS (in the case of interacting hyperons – to softening of the EoS), see Fig. 6(c), and to smaller masses and radii of the stars, see Fig. 7(c).

For YY interactions, represented by the potential $V_\Lambda^{(A)}(\rho_0/5)$, the situation is rather clear: deeper potentials yield softer EoSs. Note that the variation of $V_\Lambda^{(A)}(\rho_0/5)$ do not affect the onset of Λ which is essentially determined by $V_\Lambda^{(N)}(\rho_0)$ but they do affect the abundance of these species. Varying the value of $V_\Lambda^{(A)}(\rho_0/5)$ by 20% changes the maximum mass of corresponding stars by only about $0.01 M_\odot$. For a larger variation of 200% we find that the maximum mass varies in the range $1.72 \leq M/M_\odot \leq 1.82$, see panels (d) of Figs. 6 and 7.

Finally, we would like to illustrate the effects of Lorentz tensor couplings on the mass-radius relations of neutron stars. In Fig. 7(d) we show also the case where the vector meson- Y tensor couplings are set to zero. In this case we observe that the maximum mass shifts up by about $0.06 M_\odot$.

Because EoS represents the sum of contributions from each baryons (and leptons), we varied so far their potentials in turn, to see the amount of changes associated with each baryon. These variations can be better understood if one examines the particle fractions corresponding to those EoSs, which are shown in Fig. 8 for selected values of potential depths.

Firstly, comparing panels (a) and (b) of Fig. 8, we find that a less deep potential $V_\Lambda^{(N)}(\rho_0)$ pushes up the threshold density of Λ , while the onsets of $\Xi^{-,0}$ shift down in density and the

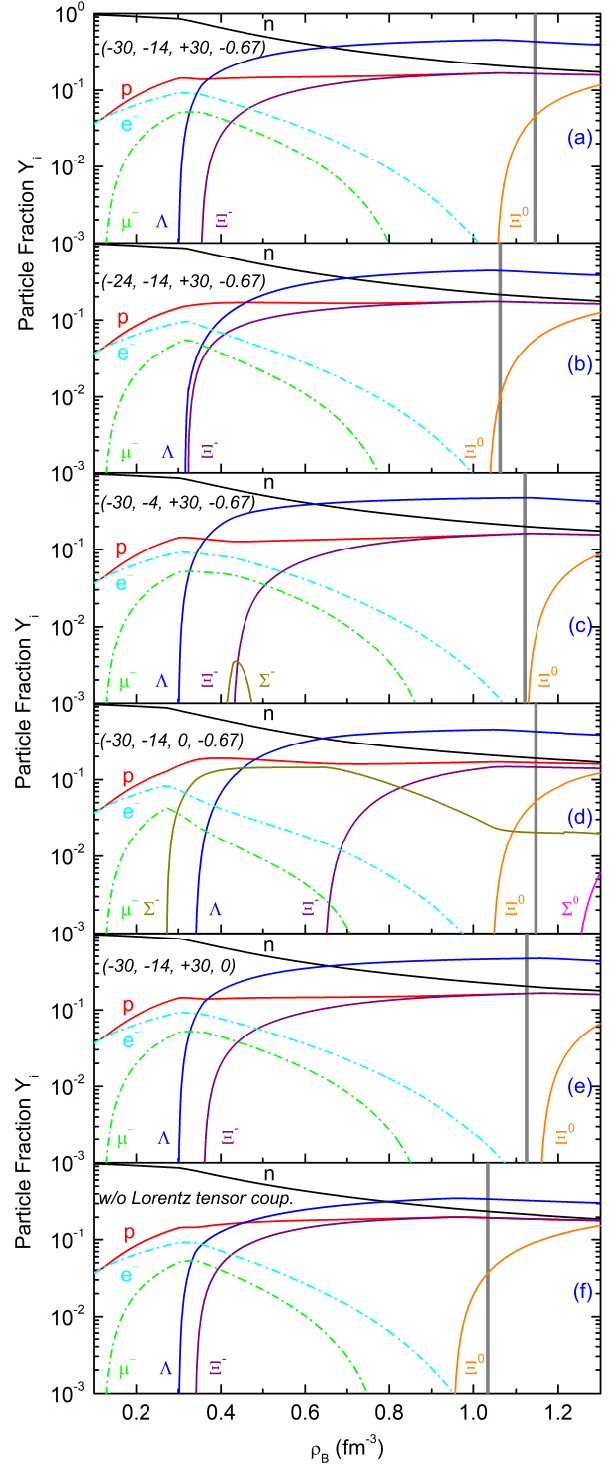


Fig. 8. Particle fractions of hyperonic matter for different values of isoscalar hypernuclear potentials in nuclear matter $V_Y^{(N)}(\rho_0)$ and hyperonic potentials in hyperonic matter $V_\Lambda^{(A)}(\rho_0/5)$. We tune the coupling constants $\sigma(\sigma^*)-Y$ while the others are fixed according to the SU(6) symmetric model. (a) $V_Y \equiv (V_\Lambda^{(N)}, V_\Xi^{(N)}, V_\Sigma^{(N)}, V_\Lambda^{(A)}) = (-30, -14, +30, -0.67)$ MeV; (b) $V_Y = (-24, -14, 30, -0.67)$ MeV; (c) $V_Y = (-30, -4, 30, -0.67)$ MeV; (d) $V_Y = (-30, -14, 0, -0.67)$ MeV; (e) $V_Y = (-30, -14, +30, 0)$ MeV; (f) same as (a) but switch off the Lorentz tensor (LT) couplings. The thick vertical lines indicate the central density of the respective maximum mass configurations. The results are calculated using the RHF DF with PKO3 parameterization.

overall fraction of particles vary to some extent. Similarly, a less deep potential $V_{\Xi}^{(N)}(\rho_0)$ pushes up the threshold densities of $\Xi^{-,0}$, while new specie Σ^- could arise, see panel (c). We see that if one type of hyperon is pushed up in density by the change of their potential, a different hyperon takes its place; due to this compensation mechanism the variations in the $\Lambda(\Xi)$ potentials do not affect the EoS substantially. For example, as discussed above, the 20% variation in the $V_{\Lambda}^{(N)}(\rho_0)$ results in the variation in the maximum mass and the radius of hyperonic stars by $0.04M_{\odot}$ and 0.50 km respectively.

Secondly, comparing panels (a) and (d) of Fig. 8 we notice that the change in the Σ^- potential can drastically change their onset density and matter composition. Indeed in panel (a) where the Σ^- potential is large and positive it is completely absent from matter composition, whereas in panel (d) where its potential is zero it is the first hyperon to appear. In this case Σ^- populates matter up to densities of about $4\rho_0$ where Ξ^- sets in at a similar density as in the case of repulsive $V_{\Sigma}^{(N)}(\rho_0) = 30$ MeV. At higher density, Ξ^- essentially replaces Σ^- . Thus, we conclude that Σ^- , if it appears, it will affect the intermediate density region ($3 \sim 5\rho_0$) of the EoS.

Next, comparing the panels (a) and (e) of Fig. 8 we find that the variation of YY interaction for Λ particles does not change their onset density, but modify their fraction. We note that according to Eq. (33) any reduction $g_{\sigma^*\Lambda}$ leads to a reduction of $g_{\sigma^*\Xi}$ and $g_{\sigma^*\Sigma}$. Therefore, the threshold densities for Ξ s are higher (which is more notable for Ξ^0 s) and their abundances are overall decreased. (The same would apply to Σ^- if the parameter choice allows for their appearance).

Finally we study the effect of the Lorentz tensor coupling (present only in the HF computations) by comparing panel (a) to panel (e) of Fig. 8, in which this coupling has been set to zero. We find that the overall attraction provided by the vector meson-hyperon tensor couplings shifts down the onsets of Ξ^- s, and reduces the abundances of hyperons. It is thus clear that the tensor couplings, which contribute only through the Fock diagrams, have an important effect on the particle populations in dense matter.

In conclusion, we find that the variations of hyperon potentials change the threshold densities at which the hyperons appear. We also observe that the particle fractions vary depending on the magnitude of the potentials, especially the appearance of Σ^- crucially depends on the value of its potential. In addition we find a compensation mechanism which shows that when the Λ particles are disfavored, then the Ξ^- hyperons replace them, thus keeping the total amount of strangeness in matter at the same level. As a consequence, the variations of particle fractions do not affect the global properties of stars, i.e. their maximum mass and the corresponding radius. Note however, that the inclusion of YY interactions has an important effect on the maximum mass.

The maximum masses obtained from our models so far do not satisfy the lower bound on the maximum mass $M \sim 2M_{\odot}$ of compact stars set by the observations of PSR J0348+0432 and PSR J1614-2230. The ways to overcome this difficulty suggested in the literature include: (a) reduction of the strength of the hyperon coupling to meson [37, 38], (b) increase in the hyperon potentials $U_Y^{(N)}$ [28, 36], or (c) modifying the values of the hyperon couplings away from the values implied SU(6)

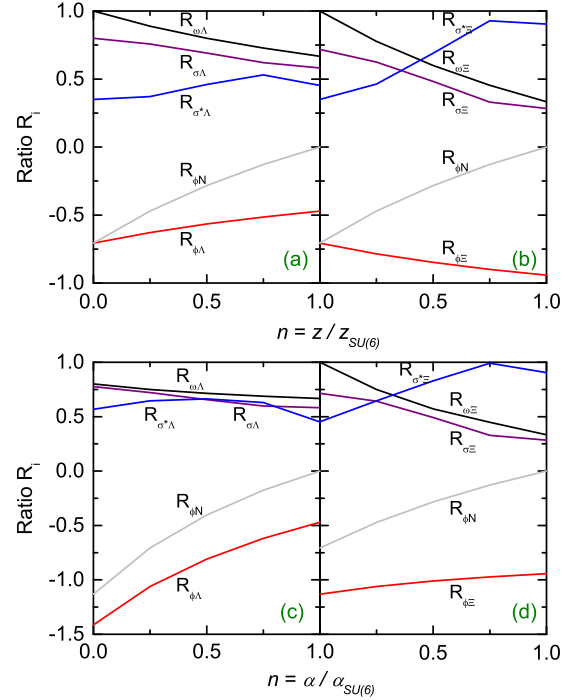


Fig. 9. Relative coupling strengths for Λ hyperon (panels a, c) and Ξ hyperon (panels b, d) in the isoscalar channels as a function of $z(\alpha)$ and normalized to their values in SU(6) model for fixed $\alpha = 1 (z = 1/\sqrt{6})$.

symmetry [29, 125]. We will now follow the prescription (c) at the same time keeping fixed the experiment estimates of $U_Y^{(N)}(\rho_0)$ and $U_{\Lambda}^{(\Lambda)}(\rho_0/5)$ discussed above.

4.2 Stellar matter within the SU(3) symmetry

In this section, we fix the coupling constants of vector meson-hyperon interactions according to the more general SU(3) flavor symmetry in order to allow for stellar sequences which contain members with masses of the order of observed $2M_{\odot}$. For the vector meson- Y tensor couplings, represented by the ratios $\kappa_{\alpha Y}$, we will again use their SU(6) values which are listed in Table 9 of Appendix C.

4.2.1 Varying parameters z and α_v

Consider the ideal mixing case where $\theta_v = \tan^{-1}(1/\sqrt{2})$ for vector mesons. The two choices which allow us to go beyond SU(6) symmetry are the tuning of the parameters z or α_v , see Appendix C. Below we drop the subscript v for simplicity.

We first probe the effects of variation of the ratio z (which corresponds to variation of the coupling of baryons to the meson octet g_8) on the stiffness of the hadronic EoS and corresponding mass-radius relation. We restrict z to the interval $z \in [0, 1/\sqrt{6}]$, where the upper bound corresponds to the SU(6) value. We do not consider values larger than this upper bound because the larger the z value the softer is the EoS.

We now consider the relative couplings ratios defined by the relation $R_{\alpha Y} = g_{\alpha Y}/g_{\alpha N}$; the corresponding values in the

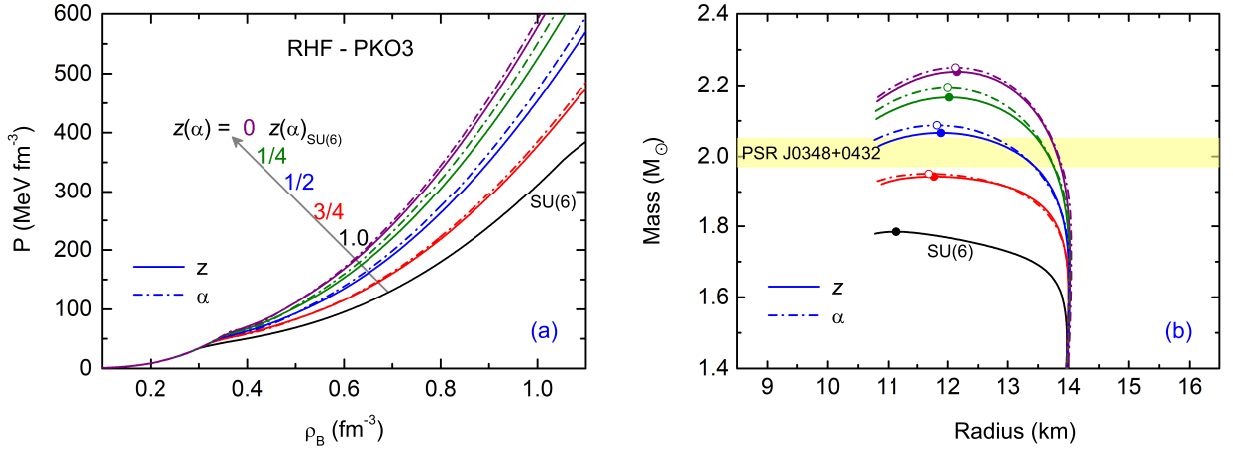


Fig. 10. Equation of state of hypernuclear matter (a) and mass-radius relation (b) within different value of $z(\alpha)$ under the SU(3) flavor symmetry. The coupling constants $\sigma(\sigma^*)$ - Y for each case are fitted by the isoscalar hypernuclear potentials $V_Y(\rho_0) \equiv (V_\Lambda^{(N)}, V_\Xi^{(N)}, V_\Sigma^{(N)}) = (-30, -14, +30)$ MeV and $V_\Lambda^{(\Lambda)}(\rho_0/5) = -0.67$ MeV.

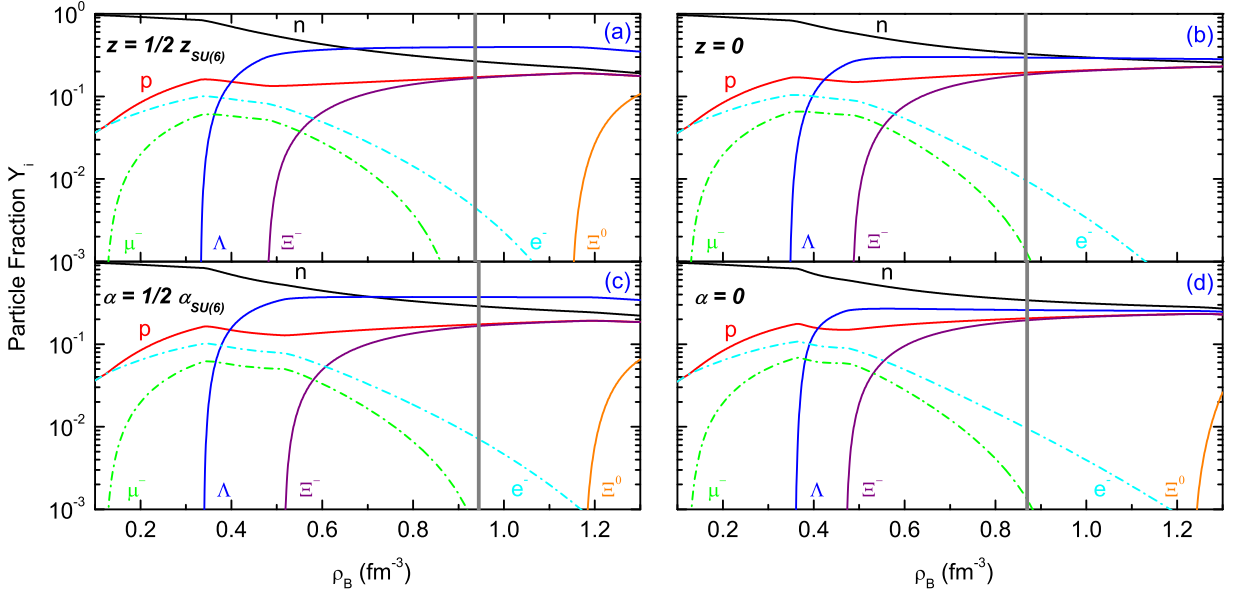


Fig. 11. Particle fractions of hypernuclear matter in the SU(3) flavor symmetric model for (a) $z = 0.5z_{SU(6)}$, (b) $z = 0$, where α is fixed to its SU(6) value, (c) $\alpha = 0.5\alpha_{SU(6)}$, (d) $\alpha = 0$, where z is fixed to its SU(6) value. The SU(6) case is given by $z_{SU(6)} = 1/\sqrt{6}$ and $\alpha_{SU(6)} = 1$. The thick vertical lines indicate the central density of the respective maximum mass configurations. The results are calculated using RHF approach with PKO3 parameterization.

case of SU(6) symmetric model are given in the Appendix C and Table 9. These ratios for Λ and Ξ as functions of z under SU(3) symmetry are shown in Fig. 9. We see that with decreasing z the ω - Λ and σ - Λ couplings increase, the ϕ - Λ couplings decrease and σ^* - Λ stays approximately constant. In the case of Ξ hyperons the coupling behave in the same manner, except the strange meson coupling σ^* - Ξ is now decreasing for $z/z_{SU(6)} \leq 0.75$ and that for ϕ - Ξ is increasing; here $z_{SU(6)} = 1/\sqrt{6}$ is the SU(6) value of the z . We see that with decreasing z the combined effect of repulsive vector meson-baryon interactions and attractive scalar meson-baryon interactions becomes more repulsive. In the case of Λ particle this is also due to the increase in the difference $R_{\omega\Lambda} - R_{\sigma\Lambda}$. The same can be said for

Ξ mesons, where in addition there is a reduction in the attractive σ^* - Ξ interaction.

The EoS for parameter values $z/z_{SU(6)} = 0, 0.25, 0.50, 0.75, 1.0$ with $\alpha = 1$ are plotted in Fig. 10(a) (in solid lines). It is seen that the EoS stiffens with decreasing z . In Fig. 10(b) we plot the corresponding mass-radius relations. As expected from the influence of z on the stiffness of the EoS, the maximum mass grows up from the value $M = 1.79M_\odot$ for $z/z_{SU(6)} = 1$ to $M = 2.24M_\odot$ for $z/z_{SU(6)} = 0$.

Now we examine at the particle fractions which are shown in Fig. 11(a, b) for $z/z_{SU(6)} = 0.5$ and 0, and compare with the SU(6) case (shown in Fig. 8(a)). In the case $z/z_{SU(6)} = 0.5$, we find that the particle composition of the core matter is the same as in the SU(6) case. On decreasing $z/z_{SU(6)}$ to 0, we find that

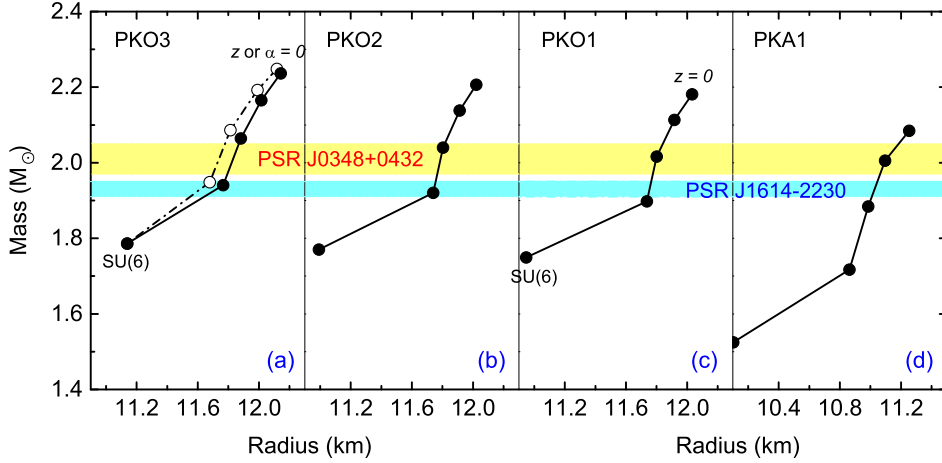


Fig. 12. The maximum masses versus radii for the hyperonic stars obtained from different RHF DF and for the range of SU(3) symmetric model values $0 \leq z \leq 1/\sqrt{6}$ (solid lines). In the case of PKO3 parameterization (panel a) we also show the same results, but for $0 \leq \alpha \leq 1$. The shaded areas show the masses of two massive pulsars, PSR J0348+0432 with $M = 2.01 \pm 0.04 M_\odot$, and PSR J1614-2230 with $M = 1.93 \pm 0.02 M_\odot$.

the onset densities of hyperons are pushed upward in density and, at the same time, their fractions decrease. We note that the onset density of Λ 's is not shifted much, since before the appearance of Λ 's in every case considered we have the same $Ne\mu$ properties together with the same constraint $V_\Lambda^{(N)}(\rho_0) = -30$ MeV.

We turn now to the examination of the effects of the ratio α on the stiffness of the hadronic EoS and mass-radius relation. We vary α in the interval $\alpha \in [0, 1]$. The relative coupling ratios for Λ and Ξ hyperons as functions of α in the SU(3) symmetric model are shown in Fig. 9. Repeating the arguments we used in the case of variations of z we see that the decrease in α has an overall repulsive effect, as expected.

The stiffness of the EoS depends monotonously on α and, again, we obtain the softest EoS for the SU(6) case (i.e., a pure F -type coupling), while the stiffest EoS is obtained for $\alpha = 0$, which corresponds to the pure D -type coupling of the meson-baryon multiples. The resulting neutron star maximum mass grows up to $M = 2.25 M_\odot$, almost coinciding with the $z = 0$ case studied above, see Fig. 10. The particle fractions for $\alpha/\alpha_{SU(6)} = 0.5$ and 0 are shown in Fig. 11(c, b).

It is interesting to observe that, working in the case of ideal mixing θ^{id} for vector mesons, tuning z or α down from their SU(6) value, yield comparable results, both for the EoS and the particle abundances.

4.2.2 Alternative parametrizations of the RHF DF

To explore the dependence of our results on the choice of the DFs, we repeated the above procedures for the remaining three sets of RHF DFT parameterization. Figure 12 shows the maximum masses and the corresponding radii of neutron stars when the z parameter is varied in the range $z \in [0, 1/\sqrt{6}]$. One can clearly see that the four parameterizations show similar trends and differ only in details. The maximum mass increases by about $0.5 M_\odot$ in the cases of PKOi ($i = 1-3$) parameterization and by $0.6 M_\odot$ in the case of PKA1 parameterization when z is varied in the range indicated above. In any event, all four

parameterization predict heavy enough ($M > 2.0 M_\odot$) compact star once SU(3) symmetry is assumed.

One may notice that the PKA1 DF is special in our collection as it predicts smaller radii than the PKOi ($i = 1-3$) DFs. The main difference between these DFs are the values of symmetry energy and slope parameter, see Table 3. As a general trend, it has been established that the radius of a compact star increase with the slope parameter L , which is opposite to the trend we see [126, 127]. However, the EoS derived from the covariant DFT is very sensitive to both the isoscalar and isovector channels. If we only focus on the symmetry energy J and the slope L of nucleonic EoS, its effect on the hyperonic EoS could be split into two pieces: on one hand, the larger L (or J) the stiffer the nucleonic sector of the EoS; on the other hand, the larger L (or J) the lower the Λ onset density and the larger the Λ fraction. This latter effect makes the EoS softer for our models in which Λ is the dominant hyperon. Therefore, in our case, it is the interplay between the above two effects that determines the properties of hyperonic EoS. Furthermore, the density dependence of the couplings in the two isoscalar channels for PKA1 parameterization is quite different from the PKOi ($i = 1-3$) parameterizations, all of which feature similar density dependences of couplings, see Refs. [54, 65]. The EoS derived from the covariant DFT is very sensitive to balance between the two isoscalar channels, therefore the resulting differences are expected.

From our detailed analysis above, we conclude that massive hyperonic neutron stars can be obtained within RHF DFT when the couplings of the SU(3) flavor symmetric model are tuned appropriately.

In closing, it is worthwhile to remark here that the canonical $1.4 M_\odot$ mass neutron stars do not contain hyperons in all models described above and their properties are entirely determined by the nuclear covariant DFT. Indeed, hyperons appear earliest in the case of soft EoS, which occurs in the SU(6) symmetric model. Even in this limiting case we find that the hyperons appear in compact stars with masses with $M > 1.5 M_\odot$, i.e., masses larger than the canonical pulsar mass.

Table 5. Isoscalar meson-hyperon coupling constants for the RHF models of dense matter which produce sequences of compact stars with massive $2M_{\odot}$ stars. We list the model the parameters specifying the SU(3) parameterization, i.e., z and α_v , the values of $R_{\sigma Y} = g_{\sigma Y}/g_{\sigma N}$ and $R_{\sigma^* Y} = g_{\sigma^* N}/g_{\sigma N}$.

DF	z	α_v	$R_{\sigma\Lambda}$	$R_{\sigma\Sigma}$	$R_{\sigma^*\Lambda}$	$R_{\sigma^*\Sigma}$	$R_{\sigma^*\Xi}$	$R_{\sigma^*\Psi}$
PKA1	$\frac{1}{4\sqrt{6}}$	1	0.7650	0.6410	0.5138	0.6134	0.7668	0.6134
PKO1	$\frac{1}{2\sqrt{6}}$	1	0.7029	0.4863	0.4157	0.3802	0.5703	0.3802
PKO2	$\frac{1}{2\sqrt{6}}$	1	0.6913	0.4790	0.4053	0.4161	0.6242	0.4161
PKO3	$\frac{5}{8\sqrt{6}}$	1	0.6561	0.4059	0.3906	0.4992	0.8112	0.4992
PKO3	$\frac{1}{\sqrt{6}}$	$\frac{5}{8}$	0.6255	0.4083	0.4711	0.6518	0.9125	0.3911

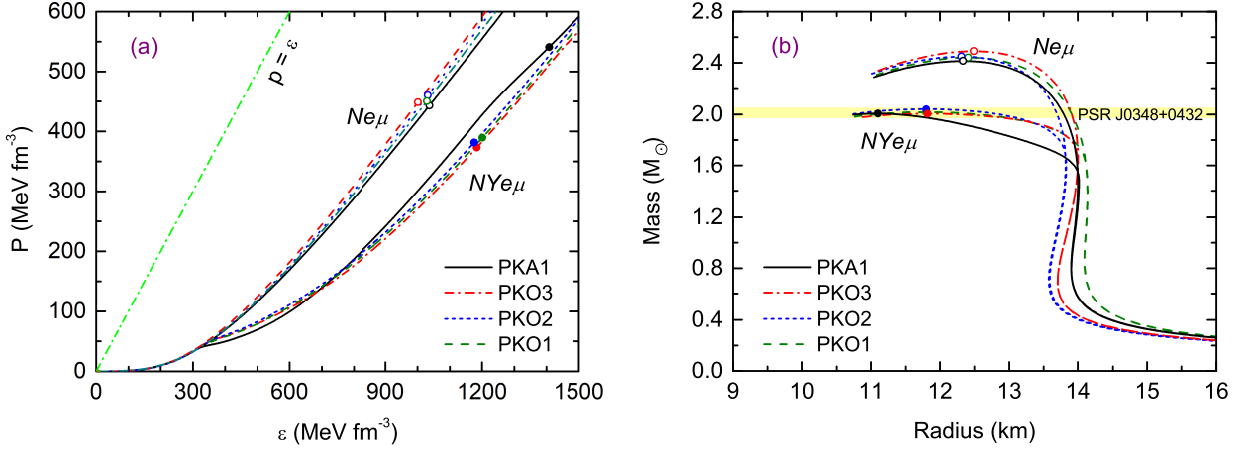


Fig. 13. Equation of state (a) and mass-radius relation (b) of hypernuclear matter ($NYe\mu$) predicted by the models that favor a maximum gravitational mass of $2.0M_{\odot}$ under SU(3) flavor symmetry. The nucleonic-only ($Ne\mu$) results are also shown. The circles shows the point at which a neutron star reaches the maximum mass. The shaded area portrays the mass of pulsar PSR J0348+0432, $2.01 \pm 0.04M_{\odot}$.

4.3 Stellar sequences with maximum mass $2M_{\odot}$ and their EoS

Next we concentrate on the models of dense matter which produce sequences of compact stars with massive $2M_{\odot}$ stars and their properties. The scalar meson-hyperon coupling constants (the ratios $R_{\sigma Y} = g_{\sigma Y}/g_{\sigma N}$ and $R_{\sigma^* Y} = g_{\sigma^* N}/g_{\sigma N}$) for the RHF DFs which were used in the following calculations are presented in Table 5. The remaining constants for vector meson-hyperon couplings can be obtained by the SU(3) relations (45) and (49) in Appendix C. These models are of practical importance as these can be used in modeling dynamics of neutron stars with hyperons on the basis of EoS which are constrained by the pulsar mass measurements.

4.3.1 The mass vs radius relations

Figures 13 (a) and (b) show the EoSs and the corresponding mass-radius relations computed with the four RHF DFs within the SU(3) symmetric model. The four parameterizations fall into two groups, one corresponding to PKO*i* ($i = 1-3$) and the other to PKA1. The maximum mass for all these DFs are at about $2.0M_{\odot}$, with the radii of this maximal mass star differing by about 1.0 km. Note that the PKA1 parameterization provides an EoS, which is softer at low density, but becomes stiffer at high density, thus allowing for $2.0M_{\odot}$ object. The central density

of this object is much higher and it is more compact than its counterparts constructed from PKO*i* ($i = 1-3$) EoSs.

Despite of similarity in the EoS predicted by these DFs, there are large differences in the internal composition of the massive stars. This is illustrated in Fig. 14, which shows particle fractions and baryon densities as a function of the radial coordinate for a $2M_{\odot}$ compact star. As expected, hyperons are concentrated in the inner core (in the region with $r \leq 8$ km) and they become the dominant component within $r \leq 6$ km, while leptons are concentrated mostly in the outer part of the star ($r \geq 6$ km). Therefore, our RHF DFs favor a strongly hyperon populated core inside massive star. An interesting feature of PKA1 DF is the appearance of Ξ^0 hyperons in the very inner part of the neutron star inner core, which occurs at the cost of slight reduction of the Λ s. It is worthwhile noting that the distribution of nucleonic component in the inner core is almost constant, and has the value roughly $2.5\rho_0$.

Finally, we summarize in Table 6 the relevant properties for a $2.0M_{\odot}$ compact star obtained with different DFs, including the strangeness fraction F_s at central densities ρ_c , the onset density of hyperons Y_0 . The radii of such stars are seen to be in the range $11.1 \sim 11.8$ km, the central densities are about $6.5\rho_0$ (see also Fig. 14), the strangeness fraction at the center is about 0.25, and the onset density for the dominant hyperon (Λ) is about $2.2\rho_0$.

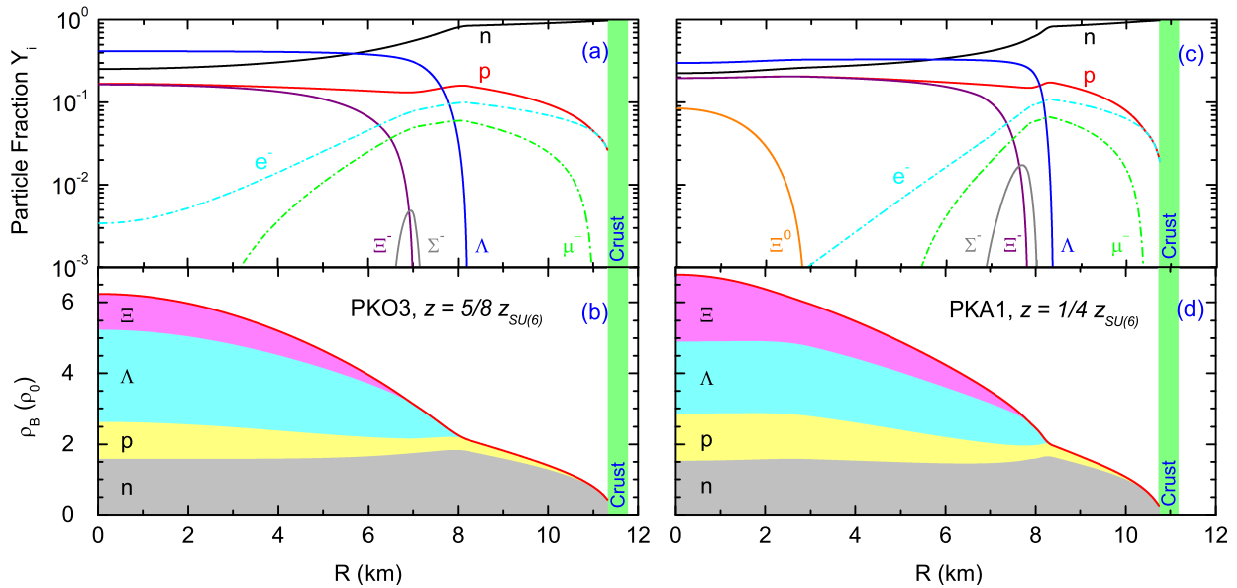


Fig. 14. Particle fractions (a, c) and baryon number density (b, d) of hyperonic matter as a function of circumferential radius in the core of a $2.0M_{\odot}$ star, which corresponds to the maximum gravitational mass of the models with the a case SU(3) flavor symmetry parameters as indicated in the figure.

Table 6. Properties for a $2.0M_{\odot}$ configurations. We list the model the parameters specifying the SU(3) parameterization, i.e., z and α_v , the mass M_{\max} (M_{\odot}), radius R_{\max} (km), central density ρ_c (fm^{-3}) and its strangeness fraction F_s (strangeness per baryon) of the maximum-mass configurations, as well as the onset densities of the appearance of hyperons Y_0 (fm^{-3}).

DF	z	α_v	M_{\max}	R_{\max}	ρ_c	$F_s(\rho_c)$	$Y_0(\Lambda)$	$Y_0(\Xi)$
PKA1	$\frac{1}{4\sqrt{6}}$	1	2.006	11.096	1.088	0.286	0.316	0.428
PKO1	$\frac{2}{\sqrt{6}}$	1	2.016	11.801	0.965	0.242	0.329	0.514
PKO2	$\frac{1}{2\sqrt{6}}$	1	2.035	11.803	0.948	0.241	0.340	0.501
PKO3	$\frac{5}{8\sqrt{6}}$	1	2.005	11.822	0.957	0.248	0.327	0.482
PKO3	$\frac{1}{\sqrt{6}}$	$\frac{5}{8}$	2.019	11.731	0.973	0.242	0.332	0.526

4.3.2 Direct Urca processes

The studies of cooling of a compact star provide important information about their interior composition. The direct Urca process on baryons, if it is kinematically allowed, is the most powerful mechanism of neutrino emission from the neutron star interior [128, 129]. Its direct and inverse versions can be written schematically as

$$B_1 \rightarrow B_2 + l + \bar{\nu}_l, \quad B_2 + l \rightarrow B_1 + \nu_l, \quad (34)$$

where B are baryons involved in the weak interaction process, l is a lepton, either an electron or a muon, and ν_l is the neutrino associated with lepton l . Simultaneous conservation of energy-momentum requires that the triangle inequality must be fulfilled for the Fermi momenta

$$|p_{B_2}^F - p_l^F| \leq p_{B_1}^F \leq p_{B_2}^F + p_l^F. \quad (35)$$

It defines the critical density above which the processes (34) are allowed. Once hyperons are present in matter, various types of hyperon direct Urca process will be allowed, because the above conditions are fulfilled already for very low fraction of hyperons, of the order of few percent. The hyperonic direct Urca

process can play an important role in the cooling history of a compact star because, they can become operative already at relatively small proton fraction at which the nucleonic direct Urca process is still forbidden [46, 130–132].

Clearly, a direct Urca process can operate in the interior of a star if its central density exceeds the critical density for this process. If allowed, such a process is operating within a spherical region with a radius corresponding to the critical density. In Fig. 15 we show the thresholds of the direct Urca processes on nucleons and hyperons as a function of density calculated for PKO3 and PKA1 parameterizations. The horizontal lines mark the masses of stars above which the corresponding process operates.

In the case of PKO3 parameterization, shown in Fig. 15(a), the nucleonic direct Urca process (np) is allowed in the central cores of all stars with $M \gtrsim 1.3M_{\odot}$. Once a hyperon is present, its concentration increases rapidly with density, and consequently the critical density for the Urca process generally differs little from the onset density. For instance, the Λ hyperon appears first at density 0.327 fm^{-3} and the direct Urca process involving Λs occurs if $\rho_B \geq 0.329 \text{ fm}^{-3}$. As a result of such low critical density for Λ , the hyperonic process (Λp) starts to act in the stars with masses $M \gtrsim 1.5M_{\odot}$. The process ($\Xi^- \Lambda$) operates only in

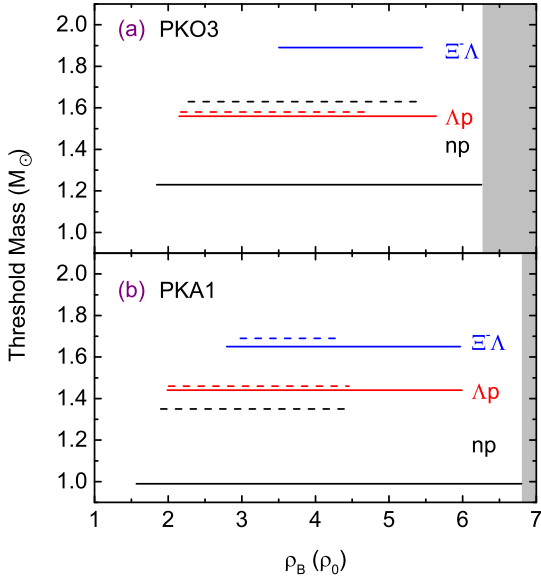


Fig. 15. The direct Urca processes in hypernuclear stars as a function of the normalized baryonic density, predicted by the two DFs that lead to a maximum gravitational mass of $2.0M_\odot$ in the SU(3) flavor symmetric model. The relevant baryons are n, p, Λ , and Ξ^- . The solid (dashed) lines denote the electron (muon) versions of the processes. The y-axis shows the mass of the star in which the threshold for a given process is achieved. The shading indicates the region beyond the maximum mass configurations.

massive stars with $M \gtrsim 1.9M_\odot$. In the case of PKA1 parameterization, the general features discussed above are intact, but the critical densities and the corresponding threshold masses are somewhat smaller, see Fig. 15(b).

At the same time, the hypernuclear processes are quenched above the density $5.5\text{--}6.0\rho_0$ due to the strong suppression of lepton concentrations, in particular the concentrations of μ -ons, see Fig. 14. The nucleonic direct Urca process which involves only electrons remains intact in a larger range of densities. This implies that in the innermost core of a massive star cools predominantly by the nucleonic direct Urca process. One should, however, notice that the emissivity of the various Urca processes is dependent on the partial concentrations of each baryon and/or lepton species, their effective masses which in turn are determined by the EoS as well as their standard model weak-couplings constant and the importance of various processes can be ultimately revealed through the cooling simulations of corresponding models.

5 Summary and conclusions

We have provided a first study of the hypernuclear matter in neutron stars with the relativistic Hartree-Fock theory using a DFT with density dependent couplings and including the full octet of baryons. This extends previous studies of hyperonization in dense matter to the level of the relativistic Hartree-Fock theories thus providing a new insight into the role played by the tensor forces, pion-exchanges, space component of vector self-energy, among other things, not revealed in the Hartree type

approaches. Our work complements previous studies of the hyperonization problem in the Hartree-Fock theories which were based exclusively on the quark-meson coupling model [50–52].

Two factors contribute to the softening of the EoS in our framework: (a) the Fock terms generically make the hypernuclear EoS soft, as they could even provide a negative contribution to the pressure; (b) the meson-hyperon tensor couplings mediate additional attraction among hyperons compared to the models based on Hartree self-energies.

We followed the strategy of previous work (see for example [28, 29, 37, 38]) to (a) use the SU(3) spin-flavor symmetric quark model to tune the hypernuclear coupling constants at fixed values of the nucleonic ones and (b) to vary the depth of hypernuclear potential. Within the parameter space of SU(3) symmetric quark model we find hypernuclear stellar configurations with masses that span from $1.7M_\odot$ to $2.2M_\odot$. Our assessment of the influence of the uncertainties of the hyperon potentials on the EoS and mass-radius relation for different underlying parametrizations of nuclear matter shows that, the variation of hyperon potentials do not change the maximum mass and the radius of a neutron star significantly due to a delicate compensation among the three types of hyperons. In particular, large changes in the Ξ and Σ potentials (e.g., 70% variations around their accepted values) do not produce significant changes in the EoS and parameters of stellar configurations. We also find that our results are not sensitive on the choice of the available nuclear DFs.

We have selected those EoSs which produce compact stars with maximum mass of the order of $2.0M_\odot$ and thus can be used in the neutron star phenomenology. For these models we have also estimated the critical density and threshold mass for hyperon direct Urca processes. Our analysis shows that once hyperons are present, the hyperon direct Urca processes become operative due to the rapid rise in the hyperon population and star with a mass $M \gtrsim 1.5M_\odot$ are very likely to cool via the hyperon direct Urca process. Furthermore, we point out that the hypernuclear direct Urca processes could be quenched above $5.5\text{--}6.0\rho_0$ due to the strong suppression of lepton concentrations.

In the future it is worthwhile to consider the baryon exchange (transition) processes which may change the particle composition, although the effects of these processes were found to be small in a recent work [133]. The hypernuclear coupling constants can be further tuned on hypernuclei instead of using the empirical potential depth of hyperons in nuclear matter. Another problem is the onset of resonances in dense matter [134, 135] and the interferences among hyperons and Λ isobars should be investigated as well [136]. A natural extension of the present baryonic EoS would be to include a deconfined quark phase at high densities.

J. L. acknowledges the support by the Alexander von Humboldt foundation. A. S. is supported by the Deutsche Forschungsgemeinschaft (Grant No. SE 1836/3-2) and by the NewCompStar COST Action MP1304. W. L. is supported by the National Natural Science Foundation of China under Grant Nos. 11375076 and 11675065.

Table 7. Functions A_α , B_α , C_α and D_α in Eq. (11).

α_i	A_α	B_α	C_α	D_α
σ_S	$g_{\alpha B}^2 \Theta_\sigma$	$g_{\alpha B}^2 \Theta_\sigma$	$-2g_{\alpha B}^2 \Phi_\sigma$	-
δ_S	$g_{\delta B}^2 \Theta_\delta$	$g_{\delta B}^2 \Theta_\delta$	$-2g_{\delta B}^2 \Phi_\delta$	-
ω_V	$2g_{\omega B}^2 \Theta_\omega$	$-4g_{\omega B}^2 \Theta_\omega$	$-4g_{\omega B}^2 \Phi_\omega$	-
ω_T	$-(f_{\omega B}/2M)^2 m_\omega^2 \Theta_\omega$	$-3(f_{\omega B}/2M)^2 m_\omega^2 \Theta_\omega$	$4(f_{\omega B}/2M)^2 m_\omega^2 \Lambda_\omega$	-
ω_{VT}	-	-	-	$12(f_{\omega B} g_{\omega B}/2M) \Omega_\omega$
ρ_V	$2g_{\rho B}^2 \Theta_\rho$	$-4g_{\rho B}^2 \Theta_\rho$	$-4g_{\rho B}^2 \Phi_\rho$	-
ρ_T	$-(f_{\rho B}/2M)^2 m_\rho^2 \Theta_\rho$	$-3(f_{\rho B}/2M)^2 m_\rho^2 \Theta_\rho$	$4(f_{\rho B}/2M)^2 m_\rho^2 \Lambda_\rho$	-
ρ_{VT}	-	-	-	$12(f_{\rho B} g_{\rho B}/2M) \Omega_\rho$
π_{PV}	$-f_{\pi B}^2 \Theta_\pi$	$-f_{\pi B}^2 \Theta_\pi$	$2f_{\pi B}^2/m_\pi^2 \Pi_\pi$	-

Note. For the strange mesons σ^* and ϕ , The functions A_α , B_α , C_α and D_α for σ^* coincide with those for σ and for ϕ coincide with ω . The index i is specified in the left column, where $S(V)[T]$ stands for the scalar(vector)[tensor] coupling at each meson-baryon vertex.

Table 8. The effective interactions PKOi ($i = 1-3$) and PKA1 of RHF DFT, where the masses are $M_N = 938.9$ MeV, $m_\omega = 783.0$ MeV, $m_\rho = 769.0$ MeV, and $m_\pi = 138.0$ MeV.

	m_σ	g_σ	g_ω	g_ρ	f_π	κ_ρ	a_ρ	a_π	$a_{\rho T}$
PKO1	525.769084	8.833239	10.729933	2.434749	0.291716	-	0.076760	1.231976	-
PKO2	534.461766	8.920597	10.550553	2.163268	-	-	0.631605	-	-
PKO3	525.667686	8.895635	10.802690	2.030285	0.392931	-	0.635336	0.934122	-
PKA1	488.227904	8.372672	11.270457	2.118421	0.310448	3.199491	0.544017	1.200000	0.820583
	a_σ	b_σ	c_σ	d_σ	a_ω	b_ω	c_ω	d_ω	ρ_0
PKO1	1.384494	1.513190	2.296615	0.380974	1.403347	2.008719	3.046686	0.330770	0.152
PKO2	1.375772	2.064391	3.052417	0.330459	1.451420	3.574373	5.478373	0.246668	0.151
PKO3	1.244635	1.566659	2.074581	0.400843	1.245714	1.645754	2.177077	0.391293	0.153
PKA1	1.103589	16.490109	18.278714	0.135041	1.126166	0.108010	0.141251	1.536183	0.160

Appendix A. Functions in the self-energy

The explicit expression for the functions A_α , B_α , C_α and D_α in Eq. (11) are given in Table 7, where, for compactness, we introduced the following short-hand notations,

$$\Theta_\alpha(p, p') \equiv \ln \frac{m_\alpha^2 + (p + p')^2}{m_\alpha^2 + (p - p')^2}, \quad (36a)$$

$$\Phi_\alpha(p, p') \equiv \frac{1}{4pp'}(p^2 + p'^2 + m_\alpha^2)\Theta_\alpha(p, p') - 1, \quad (36b)$$

$$\Pi_\alpha(p, p') \equiv (p^2 + p'^2 - \frac{m_\alpha^2}{2})\Phi_\alpha(p, p') - pp'\Theta_\alpha(p, p'), \quad (36c)$$

$$\Lambda_\alpha(p, p') \equiv (p^2 + p'^2)\Phi_\alpha(p, p') - pp'\Theta_\alpha(p, p'), \quad (36d)$$

$$\Omega_\alpha(p, p') \equiv p\Theta_\alpha(p, p') - 2p'\Phi_\alpha(p, p'). \quad (36e)$$

Appendix B. Details of nucleonic RHF parameterization

In RHF approach, the explicit density dependence is introduced into the meson-nucleon couplings in the following form

$$g_{\alpha N}(\rho_N) = g_{\alpha N}(\rho_0)\eta_\alpha(x), \quad (37)$$

where $x = \rho_B/\rho_0$, ρ_B is the baryonic density, ρ_0 is the nuclear saturation density.

In the isoscalar channels, the ansatz η_α for σ and ω mesons is given by

$$\eta_\alpha(x) = a_\alpha \frac{1 + b_\alpha(x + d_\alpha)^2}{1 + c_\alpha(x + d_\alpha)^2}, \quad \alpha = \sigma, \omega. \quad (38)$$

This function is subject to the following constraints: $\eta_{\alpha N}(1) = 1$, $\eta'_{\alpha N}(0) = 0$ and $\eta''_{\alpha N}(1) = \eta''_{\omega N}(1)$, which reduce the number of free parameters to three.

In the isovector channels, for simplicity, the density dependence is taken in an exponential form

$$f_{\alpha N}(x) = f_{\alpha N}(\rho_0)e^{-a_\alpha(x-1)}, \quad \alpha = \pi, \rho, \quad (39)$$

According to the general strategy of relativistic DFT, the masses and the couplings strengths appearing in the RHF Lagrangian (1) have been determined through fits to the masses of reference nuclei and the bulk properties of symmetric nuclear matter at the saturation. The parameters of the RHF effective interactions PKOi ($i = 1-3$) and PKA1 are shown in Table 8.

Appendix C. SU(3) flavor symmetry model

The NY and YY interactions are currently not determined due to the lack of sufficiently abundant and accurate experimental data. This makes understanding the hyperonic sector a long-standing theoretical challenge. One possible approach to this sector is the use of the symmetries underlying the quark

Table 9. Values of $R_{\alpha Y} = g_{\alpha Y}/g_{\alpha N}$ and $\kappa_{\alpha Y} = f_{\alpha Y}/g_{\alpha Y}$ for hyperons within the SU(6) spin-flavor relations.

$R \setminus Y$	Λ	Σ	Ξ
$R_{\sigma Y}$	2/3	2/3	1/3
$R_{\sigma^* Y}$	$-\sqrt{2}/3$	$-\sqrt{2}/3$	$-2\sqrt{2}/3$
$R_{\omega Y}$	2/3	2/3	1/3
$\kappa_{\omega Y}$	-1	$1 + 2\kappa_{\omega N}$	$-2 - \kappa_{\omega N}$
$R_{\phi Y}$	$-\sqrt{2}/3$	$-\sqrt{2}/3$	$-2\sqrt{2}/3$
$\kappa_{\phi Y}$	$2 + 3\kappa_{\omega N}$	$-2 - \kappa_{\omega N}$	$1 + 2\kappa_{\omega N}$
$R_{\rho Y}$	0	2	1
$\kappa_{\rho Y}$	0	$-3/5 + (2/5)\kappa_{\rho N}$	$-6/5 - (1/5)\kappa_{\rho N}$
$f_{\pi Y}$	0	$2\alpha_{ps}$	$-(1/2)\alpha_{ps}$

Note. $\alpha_{ps} = 0.40$, see Refs. [101, 102]. κ denotes the ratio of the tensor to vector couplings of the vector mesons.

model of hadrons. The SU(3) symmetry in flavor space is commonly regarded as an approximate symmetry group of strong interaction if one restricts the attention only on three lightest quark flavors (up, down, and strange).

The SU(3) invariant Lagrangian can be constructed using matrix representations for the baryons B , and meson nonet (singlet state M_1 , and octet state M_8). In this work we consider the lowest order baryon octet ($J^P = 1/2^+$). The SU(3) interaction Lagrangian is a linear combinations of the antisymmetric (F -type), symmetric (D -type), and singlet (S -type) scalars,

$$\begin{aligned} \mathcal{L}_{\text{int}} = & -g_8 \sqrt{2} [\alpha \text{Tr}(\{\bar{B}, M_8\}B) + (1 - \alpha) \text{Tr}(\{\bar{B}, M_8\}B)] \\ & - g_1 \frac{1}{\sqrt{3}} \text{Tr}(\bar{B}B) \text{Tr}(M_1). \end{aligned} \quad (40)$$

Here, g_8 and g_1 denote the meson octet and singlet coupling constant respectively, the parameter α , known as $F/(F + D)$ ratio, lies in the range $0 \leq \alpha \leq 1$.

Considering the vector meson sector, the combinations of the unphysical SU(3) singlet, $|1\rangle$, and octet, $|8\rangle$, states produces the physical ω and ϕ mesons

$$\omega = \sin \theta_v |8\rangle + \cos \theta_v |1\rangle, \quad (41a)$$

$$\phi = \cos \theta_v |8\rangle - \sin \theta_v |1\rangle, \quad (41b)$$

with θ_v being the mixing angle. The coupling constants of the physical vector mesons with the baryons read as follows:

$$g_{\omega N} = \cos \theta_v g_1 + \sin \theta_v (4\alpha_v - 1) g_8 / \sqrt{3}, \quad (42a)$$

$$g_{\omega \Lambda} = \cos \theta_v g_1 - 2 \sin \theta_v (1 - \alpha_v) g_8 / \sqrt{3}, \quad (42b)$$

$$g_{\omega \Sigma} = \cos \theta_v g_1 + 2 \sin \theta_v (1 - \alpha_v) g_8 / \sqrt{3}, \quad (42c)$$

$$g_{\omega \Xi} = \cos \theta_v g_1 - \sin \theta_v (1 + 2\alpha_v) g_8 / \sqrt{3}. \quad (42d)$$

One could clearly see that, all possible combinations of the couplings are determined by four parameters. From these re-

lations one obtains

$$\frac{g_{\omega \Lambda}}{g_{\omega N}} = \frac{1 - \frac{2z}{\sqrt{3}}(1 - \alpha_v) \tan \theta_v}{1 - \frac{z}{\sqrt{3}}(1 - 4\alpha_v) \tan \theta_v}, \quad (43a)$$

$$\frac{g_{\omega \Xi}}{g_{\omega N}} = \frac{1 - \frac{z}{\sqrt{3}}(1 + 2\alpha_v) \tan \theta_v}{1 - \frac{z}{\sqrt{3}}(1 - 4\alpha_v) \tan \theta_v}, \quad (43b)$$

$$\frac{g_{\omega \Sigma}}{g_{\omega N}} = \frac{1 + \frac{2z}{\sqrt{3}}(1 - \alpha_v) \tan \theta_v}{1 - \frac{z}{\sqrt{3}}(1 - 4\alpha_v) \tan \theta_v}. \quad (43c)$$

The corresponding results for the ϕ -meson couplings follow from those for ω meson via the replacement $\cos \theta_v \rightarrow -\sin \theta_v$ and $\sin \theta_v \rightarrow \cos \theta_v$. An additional new term is given by

$$\frac{g_{\phi N}}{g_{\omega N}} = -\frac{\tan \theta_v + \frac{z}{\sqrt{3}}(1 - 4\alpha_v)}{1 - \frac{z}{\sqrt{3}}(1 - 4\alpha_v) \tan \theta_v}. \quad (44)$$

For the isovector meson ρ , one has

$$\frac{g_{\rho \Lambda}}{g_{\rho N}} = 0, \quad (45a)$$

$$\frac{g_{\rho \Xi}}{g_{\rho N}} = 2\alpha_v - 1, \quad (45b)$$

$$\frac{g_{\rho \Sigma}}{g_{\rho N}} = 2\alpha_v. \quad (45c)$$

Note that for $\alpha_v = 0(0.5)$, the couplings $g_{\rho \Sigma}(g_{\rho \Xi})$ are zero, although there are no physical reasons for them to be so. Such values of the couplings in practice do not affect our results. For example, for the range of coupling values $0 \leq g_{\rho \Xi} \leq 1$, the remaining meson- Y couplings being fixed to their values, we find that the variations in the EoS and mass-radius relation are negligible. This is because the ρ couplings depend exponentially on density, therefore, the ρ field is largely suppressed at high densities important for neutron stars.

The ϕ meson taken as pure $\bar{s}s$ state leads to the *ideal* mixing

$$\theta_v^{\text{id.}} = \tan^{-1}(1/\sqrt{2}). \quad (46)$$

If one determines the vector meson-baryon couplings on the basis of the assumption that nucleons do not couple to ϕ meson, then

$$z \equiv g_8/g_1 = 1/\sqrt{6}. \quad (47)$$

If we further require the universality assumption for the (electric) $F/(F + D)$ ratio, we have $\alpha_v = 1$, i.e., only the F -type coupling remains and the coupling constants are related as in the additive quark model.

In the case of the scalar mesons σ and σ^* , the coupling are given by expressions entirely analogous to those of ω and ϕ , respectively, with the replacements $\omega \rightarrow \sigma$, $\phi \rightarrow \sigma^*$. In addition the vector subscripts are changed to scalar ones, i.e., $v \rightarrow s$.

Furthermore, there is another type of couplings between the vector mesons and the baryon current $\{8\} \otimes \{8\}$ via the tensor coupling with coupling constants f^T . In order to obtain also relations for the tensor coupling constants, the corresponding SU(3) relations are in fact applied to the magnetic coupling

G^M . Using the vector dominance assumption with ideal mixing, one finds, for example, for the ω meson

$$G_{\omega\Lambda}^M = 0, \quad G_{\omega\Sigma}^M = \frac{4}{3}G_{\omega N}^M, \quad G_{\omega\Xi}^M = -\frac{1}{3}G_{\omega N}^M. \quad (48)$$

The tensor-to-vector coupling ratio κ of a baryon is then given in the static limit $G^M = g^V + f^T$. We summarize the hyperon-meson coupling ratios $R_{\alpha Y} = g_{\alpha Y}/g_{\alpha N}$ under the SU(6) spin-flavor model in Table 9, where we show only the coupling constants relevant for our model. Notice that the effective coupling of the ρ meson to the Σ hyperon (isospin $\tau = 1$) is twice that to the nucleon (isospin $\tau = 1/2$), as required by the symmetries assumed.

If we set α_v to its SU(6) value $\alpha_v = 1$ and use ideal mixing (46) while keeping z as a free parameter, we obtain

$$\frac{g_{\phi N}}{g_{\omega N}} = \frac{\sqrt{6z} - 1}{\sqrt{2} + \sqrt{3z}}, \quad (49a)$$

$$\frac{g_{\omega\Lambda}}{g_{\omega N}} = \frac{g_{\omega\Sigma}}{g_{\omega N}} = \frac{\sqrt{2}}{\sqrt{2} + \sqrt{3z}}, \quad (49b)$$

$$\frac{g_{\omega\Xi}}{g_{\omega N}} = \frac{\sqrt{2} - \sqrt{3z}}{\sqrt{2} + \sqrt{3z}}, \quad (49c)$$

$$\frac{g_{\phi\Lambda}}{g_{\omega N}} = \frac{g_{\phi\Sigma}}{g_{\omega N}} = -\frac{1}{\sqrt{2} + \sqrt{3z}}, \quad (49d)$$

$$\frac{g_{\phi\Xi}}{g_{\omega N}} = -\frac{1 + \sqrt{6z}}{\sqrt{2} + \sqrt{3z}}. \quad (49e)$$

Another choice is to set z to its SU(6) value $z = 1/\sqrt{6}$ and use the ideal mixing (46) while keeping α_v as a free parameter instead. As demonstrated in the main body of this work the two alternatives lead to similar results although the underlying physical assumptions differ.

References

1. N. K. Glendenning, *Compact Stars: Nuclear Physics, Particle Physics, and General Relativity*, Astronomy and astrophysics library (Springer, 1997).
2. F. Weber, *Pulsars as astrophysical laboratories for nuclear and particle physics* (Institute of Physics, Bristol, 1999).
3. J. Lattimer and M. Prakash, *Science* **304**, 536 (2004).
4. F. Weber, R. Negreiros, P. Rosenfield, and M. Stejner, *Prog. Part. Nucl. Phys.* **59**, 94 (2007).
5. A. Sedrakian, *Prog. Part. Nucl. Phys.* **58**, 168 (2007).
6. M. Oertel, M. Hempel, T. Klähn, and S. Typel, *Rev. Mod. Phys.* **89**, 015007 (2017).
7. P. C. C. Freire, C. G. Bassa, N. Wex, I. H. Stairs, D. J. Champion, et al., *MNRAS* **412**, 2763 (2011).
8. P. B. Demorest, T. Pennucci, S. M. Ransom, M. S. E. Roberts, and J. W. T. Hessels, *Nature* **467**, 1081 (2010).
9. E. Fonseca, T. T. Pennucci, J. A. Ellis, I. H. Stairs, D. J. Nice, et al., *Astrophys. J.* **832**, 167 (2016).
10. J. Antoniadis, P. C. C. Freire, N. Wex, T. M. Tauris, R. S. Lynch, et al., *Science* **340**, 6131 (2013).
11. J. M. Lattimer and M. Prakash, *Phys. Rep.* **621**, 127 (2016).
12. J. M. Lattimer and A. W. Steiner, *Astrophys. J.* **784**, 123 (2014).
13. A. L. Watts, N. Andersson, D. Chakrabarty, M. Feroci, K. Hebeler, et al., *Rev. Mod. Phys.* **88**, 021001 (2016).
14. A. W. Steiner, J. M. Lattimer, and E. F. Brown, *Eur. Phys. J. A* **52**, 18 (2016).
15. A. Steiner, C. Heinke, S. Bogdanov, C. Li, W. Ho, A. Bahramian, and S. Han, *Mon. Not. R. Astron. Soc.* **476**, 421 (2018).
16. K. Gendreau, Z. Arzoumanian, et al., in *American Astronomical Society Meeting* (2017), vol. 229.
17. A. Bauswein and H.-T. Janka, *Phys. Rev. Lett.* **108**, 011101 (2012).
18. B. D. Lackey and L. Wade, *Phys. Rev. D* **91**, 043002 (2015).
19. B. Abbott et al. (Virgo, LIGO Scientific), *Phys. Rev. Lett.* **119**, 161101 (2017).
20. E. Annala, T. Gorda, A. Kurkela, and A. Vuorinen, *Phys. Rev. Lett.* **120**, 172703 (2018).
21. V. Paschalidis, K. Yagi, D. Alvarez-Castillo, D. B. Blaschke, and A. Sedrakian, *Phys. Rev. D* **97**, 084038 (2018).
22. P.-G. Reinhard, *Rep. Prog. Phys.* **52**, 439 (1989).
23. P. Ring, *Prog. Part. Nucl. Phys.* **37**, 193 (1996).
24. B. D. Serot and J. D. Walecka, *Int. J. Mod. Phys. E* **6**, 515 (1997).
25. D. Vretenar, A. V. Afanasjev, G. A. Lalazissis, and P. Ring, *Phys. Rep.* **409**, 101 (2005).
26. J. Meng, H. Toki, S.-G. Zhou, S. Zhang, W. Long, and L. Geng, *Prog. Part. Nucl. Phys.* **57**, 470 (2006).
27. L. Bonanno and A. Sedrakian, *Astron. Astrophys.* **539**, A16 (2012).
28. S. Weissenborn, D. Chatterjee, and J. Schaffner-Bielich, *Nucl. Phys. A* **881**, 62 (2012).
29. S. Weissenborn, D. Chatterjee, and J. Schaffner-Bielich, *Phys. Rev. C* **85**, 065802 (2012).
30. I. Bednarek, P. Haensel, J. Zdunik, M. Bejger, and R. Mańka, *Astron. Astrophys.* **543**, A157 (2012).
31. M. E. Gusakov, P. Haensel, and E. M. Kantor, *Mon. Not. R. Astron. Soc.* **439**, 318 (2014).
32. D. Chatterjee and I. Vidña, *Europ. Phys. J. A* **52**, 29 (2016).
33. K. Maslov, E. Kolomeitsev, and D. Voskresensky, *Phys. Lett. B* **748**, 369 (2015).
34. L. Tolos, M. Centelles, and A. Ramos, *Astrophys. J.* **834**, 3 (2017).
35. W. M. Spinella, Ph.D. thesis, The Claremont Graduate University (2017).
36. W. H. Long, B. Y. Sun, K. Hagino, and H. Sagawa, *Phys. Rev. C* **85**, 025806 (2012).
37. G. Colucci and A. Sedrakian, *Phys. Rev. C* **87**, 055806 (2013).
38. E. van Dalen, G. Colucci, and A. Sedrakian, *Phys. Lett. B* **734**, 383 (2014).
39. G. Colucci and A. Sedrakian, *J. Phys. Conf. Series* **496**, 012003 (2014).

40. S. Banik, M. Hempel, and D. Bandyopadhyay, *Astrophys. J. Suppl.* **214**, 22 (2014).
41. R. O. Gomes, V. Dexheimer, S. Schramm, and C. A. Z. Vasconcellos, *Astrophys. J.* **808**, 8 (2015).
42. P. Char, S. Banik, and D. Bandyopadhyay, *Astrophys. J.* **809**, 116 (2015).
43. M. Oertel, C. Providência, F. Gulminelli, and A. R. Raduta, *J. Phys. G* **42**, 075202 (2015).
44. M. Oertel, F. Gulminelli, C. Providência, and A. R. Raduta, *Euro. Phys. J. A* **52**, 50 (2016).
45. M. Marques, M. Oertel, M. Hempel, and J. Novak, *Phys. Rev. C* **96**, 045806 (2017).
46. A. R. Raduta, A. Sedrakian, and F. Weber, *Mon. Not. R. Astron. Soc.* **475**, 4347 (2018).
47. M. Fortin, S. S. Avancini, C. Providência, and I. Vidaña, *Phys. Rev. C* **95**, 065803 (2017).
48. K. Saito, K. Tsushima, and A. W. Thomas, *Prog. Part. Nucl. Phys.* **58**, 1 (2007).
49. J. Rikovska Stone, P. A. M. Guichon, H. H. Matevosyan, and A. W. Thomas, *Nucl. Phys. A* **792**, 341 (2007).
50. E. Massot, J. Margueron, and G. Chanfray, *EPL (Europhys. Lett.)* **97**, 39002 (2012).
51. D. L. Whittenbury, J. D. Carroll, A. W. Thomas, K. Tsushima, and J. R. Stone, *Phys. Rev. C* **89**, 065801 (2014).
52. T. Miyatsu, M.-K. Cheoun, and K. Saito, *Astrophys. J.* **813**, 135 (2015).
53. W.-H. Long, N. Van Giai, and J. Meng, *Phys. Lett. B* **640**, 150 (2006).
54. W. H. Long, H. Sagawa, N. V. Giai, and J. Meng, *Phys. Rev. C* **76**, 034314 (2007).
55. H. Liang, N. Van Giai, and J. Meng, *Phys. Rev. Lett.* **101**, 122502 (2008).
56. W. H. Long, P. Ring, N. V. Giai, and J. Meng, *Phys. Rev. C* **81**, 024308 (2010).
57. W. H. Long, P. Ring, J. Meng, N. Van Giai, and C. A. Bertulani, *Phys. Rev. C* **81**, 031302 (2010).
58. J. J. Li, W. H. Long, J. Margueron, and N. Van Giai, *Phys. Lett. B* **732**, 169 (2014).
59. J. J. Li, J. Margueron, W. H. Long, and N. Van Giai, *Phys. Rev. C* **92**, 014302 (2015).
60. W. Long, H. Sagawa, J. Meng, and N. Van Giai, *Europhys. Lett.* **82**, 12001 (2008).
61. W. H. Long, T. Nakatsukasa, H. Sagawa, J. Meng, H. Nakada, and Y. Zhang, *Phys. Lett. B* **680**, 428 (2009).
62. J. J. Li, W. H. Long, J. L. Song, and Q. Zhao, *Phys. Rev. C* **93**, 054312 (2016).
63. L. J. Jiang, S. Yang, B. Y. Sun, W. H. Long, and H. Q. Gu, *Phys. Rev. C* **91**, 034326 (2015).
64. J. J. Li, J. Margueron, W. H. Long, and N. Van Giai, *Phys. Lett. B* **753**, 97 (2016).
65. B. Y. Sun, W. H. Long, J. Meng, and U. Lombardo, *Phys. Rev. C* **78**, 065805 (2008).
66. J. Götz, J. Ramschütz, F. Weber, and M. Weigel, *Phys. Lett. B* **226**, 213 (1989).
67. S. Marcos, J.-F. Mathiot, M. Lopez-Quelle, R. Niembro, and P. Bernardos, *Nucl. Phys. A* **600**, 529 (1996).
68. R. C. Tolman, *Phys. Rev.* **55**, 364 (1939).
69. J. R. Oppenheimer and G. M. Volkoff, *Phys. Rev.* **55**, 374 (1939).
70. G. Baym, C. Pethick, and P. Sutherland, *Astrophys. J.* **170**, 299 (1971).
71. G. Baym, H. A. Bethe, and C. J. Pethick, *Nucl. Phys. A* **175**, 225 (1971).
72. M. Fortin, C. Providência, A. R. Raduta, F. Gulminelli, J. L. Zdunik, P. Haensel, and M. Bejger, *Phys. Rev. C* **94**, 035804 (2016).
73. K. Hebeler, J. Lattimer, C. J. Pethick, and A. Schwenk, *Astrophys. J.* **773**, 11 (2013).
74. M. B. Tsang, Y. Zhang, P. Danielewicz, M. Famiano, Z. Li, W. G. Lynch, and A. W. Steiner, *Phys. Rev. Lett.* **102**, 122701 (2009).
75. P. Russotto, P. Z. Wu, M. Zoric, M. Chartier, Y. Leifels, R. C. Lemmon, Q. Li, J. Łukasik, A. Pagano, P. Pawłowski, et al., *Phys. Lett. B* **697**, 471 (2011).
76. P. Russotto, S. Gannon, S. Kupny, P. Lasko, L. Acosta, et al., *Phys. Rev. C* **94**, 034608 (2016).
77. P. Danielewicz and J. Lee, *Nuclear Physics A* **922**, 1 (2014).
78. G. A. Lalazissis, T. Nikšić, D. Vretenar, and P. Ring, *Phys. Rev. C* **71**, 024312 (2005).
79. N. K. Glendenning and S. A. Moszkowski, *Phys. Rev. Lett.* **67**, 2414 (1991).
80. S. Typel and H. H. Wolter, *Nucl. Phys. A* **656**, 331 (1999).
81. S. Typel, *Phys. Rev. C* **71**, 064301 (2005).
82. S. Typel, G. Röpke, T. Klähn, D. Blaschke, and H. H. Wolter, *Phys. Rev. C* **81**, 015803 (2010).
83. T. Klähn, D. Blaschke, S. Typel, E. N. E. van Dalen, A. Faessler, et al., *Phys. Rev. C* **74**, 035802 (2006).
84. W. Long, J. Meng, N. V. Giai, and S.-G. Zhou, *Phys. Rev. C* **69**, 034319 (2004).
85. T. Nikšić, D. Vretenar, P. Finelli, and P. Ring, *Phys. Rev. C* **66**, 024306 (2002).
86. X. Roca-Maza, X. Viñas, M. Centelles, P. Ring, and P. Schuck, *Phys. Rev. C* **84**, 054309 (2011).
87. Y. Sugahara and H. Toki, *Nucl. Phys. A* **579**, 557 (1994).
88. H. Toki, D. Hirata, Y. Sugahara, K. Sumiyoshi, and I. Tanihata, *Nucl. Phys. A* **588**, 357c (1995).
89. G. A. Lalazissis, J. König, and P. Ring, *Phys. Rev. C* **55**, 540 (1997).
90. G. A. Lalazissis, S. Karatzikos, R. Fossion, D. P. Arteaga, A. V. Afanasjev, and P. Ring, *Phys. Lett. B* **671**, 36 (2009).
91. B. G. Todd-Rutel and J. Piekarewicz, *Phys. Rev. Lett.* **95**, 122501 (2005).
92. W.-C. Chen and J. Piekarewicz, *Phys. Rev. C* **90**, 044305 (2014).
93. F. J. Fattoyev, C. J. Horowitz, J. Piekarewicz, and G. Shen, *Phys. Rev. C* **82**, 055803 (2010).
94. A. W. Steiner, M. Hempel, and T. Fischer, *Astrophys. J.* **774**, 17 (2013).
95. I. Tews, J. M. Lattimer, A. Ohnishi, and E. E. Kolomeitsev, *Astrophys. J.* **848**, 105 (2017).
96. E. Chabanat, P. Bonche, P. Haensel, J. Meyer, and R. Schaeffer, *Nucl. Phys. A* **635**, 231 (1998).
97. P.-G. Reinhard, *Nucl. Phys. A* **649**, 305c (1999).

98. T. Nikšić, T. Marketin, D. Vretenar, N. Paar, and P. Ring, *Phys. Rev. C* **71**, 014308 (2005).
99. T. Marketin, D. Vretenar, and P. Ring, *Phys. Rev. C* **75**, 024304 (2007).
100. E. van Dalen, C. Fuchs, and A. Faessler, *Phys. Rev. Lett.* **95**, 022302 (2005).
101. J. J. de Swart, *Rev. Mod. Phys.* **35**, 916 (1963).
102. C. B. Dover and A. Gal, *Prog. Part. Nucl. Phys.* **12**, 171 (1984).
103. J. Schaffner, C. B. Dover, A. Gal, C. Greiner, D. J. Millener, and H. Stocker, *Ann. Phys.* **235**, 35 (1994).
104. J. A. Maruhn, T. Bürvenich, and D. G. Madland, *J. Comput. Phys.* **169**, 238 (2001).
105. H. Liang, P. Zhao, P. Ring, X. Roca-Maza, and J. Meng, *Phys. Rev. C* **86**, 021302 (2012).
106. T. Hasegawa, O. Hashimoto, S. Homma, T. Miyachi, T. Nagae, et al., *Phys. Rev. C* **53**, 1210 (1996).
107. H. Hotchi, T. Nagae, H. Oota, H. Noumi, M. Sekimoto, et al., *Phys. Rev. C* **64**, 044302 (2001).
108. D. J. Millener, C. B. Dover, and A. Gal, *Phys. Rev. C* **38**, 2700 (1988).
109. N. K. Glendenning, D. Von-Eiff, M. Haft, H. Lenske, and M. K. Weigel, *Phys. Rev. C* **48**, 889 (1993).
110. K. Tsushima, K. Saito, and A. W. Thomas, *Phys. Lett. B* **411**, 9 (1997).
111. C. M. Keil, F. Hofmann, and H. Lenske, *Phys. Rev. C* **61**, 064309 (2000).
112. J. Cugnon, A. Lejeune, and H.-J. Schulze, *Phys. Rev. C* **62**, 064308 (2000).
113. I. Vidaña, A. Polls, A. Ramos, and H.-J. Schulze, *Phys. Rev. C* **64**, 044301 (2001).
114. P. Khaustov, D. E. Alburger, P. D. Barnes, B. Bassalleck, A. R. Berdoz, et al. (The AGS E885 Collaboration), *Phys. Rev. C* **61**, 054603 (2000).
115. H. Noumi, P. K. Saha, D. Abe, S. Ajimura, K. Aoki, et al., *Phys. Rev. Lett.* **89**, 072301 (2002).
116. M. Kohno, Y. Fujiwara, Y. Watanabe, K. Ogata, and M. Kawai, *Phys. Rev. C* **74**, 064613 (2006).
117. T. Nagae, T. Miyachi, T. Fukuda, H. Oota, T. Tamagawa, et al., *Phys. Rev. Lett.* **80**, 1605 (1998).
118. E. Friedman and A. Gal, *Phys. Rep.* **452**, 89 (2007).
119. C. B. Dover, D. J. Millener, A. Gal, and D. H. Davis, *Phys. Rev. C* **44**, 1905 (1991).
120. S. Aoki, S. Bahk, K. Chung, S. Chung, H. Funahashi, et al., *Prog. Theor. Phys.* **85**, 1287 (1991).
121. H. Takahashi, J. K. Ahn, H. Akikawa, S. Aoki, K. Arai, et al., *Phys. Rev. Lett.* **87**, 212502 (2001).
122. J. K. Ahn, H. Akikawa, S. Aoki, K. Arai, S. Y. Bahk, et al. (E373 (KEK-PS) Collaboration), *Phys. Rev. C* **88**, 014003 (2013).
123. E. Khan, J. Margueron, F. Gulminelli, and A. R. Raduta, *Phys. Rev. C* **92**, 044313 (2015).
124. J. Margueron, E. Khan, and F. Gulminelli, *Phys. Rev. C* **96**, 054317 (2017).
125. T. Katayama, T. Miyatsu, and K. Saito, *Astrophys. J. Suppl.* **203**, 22 (2012).
126. C. J. Horowitz and J. Piekarewicz, *Phys. Rev. Lett.* **86**, 5647 (2001).
127. R. Cavagnoli, D. P. Menezes, and C. Providência, *Phys. Rev. C* **84**, 065810 (2011).
128. J. M. Lattimer, C. J. Pethick, M. Prakash, and P. Haensel, *Phys. Rev. Lett.* **66**, 2701 (1991).
129. D. Page and J. H. Applegate, *Astrophys. J.* **394**, L17 (1992).
130. P. Haensel and O. Y. Gnedin, *Astron. Astrophys.* **290**, 458 (1994).
131. C. Schaab, S. Balberg, and J. Schaffner-Bielich, *Astrophys. J.* **504**, L99 (1998).
132. S. Tsuruta, J. Sadino, A. Kobelski, M. A. Teter, A. C. Liebmann, T. Takatsuka, K. Nomoto, and H. Umeda, *Astrophys. J.* **691**, 621 (2009).
133. T. Katayama and K. Saito, *Phys. Lett. B* **747**, 43 (2015).
134. A. Drago, A. Lavagno, G. Pagliara, and D. Pigato, *Euro. Phys. J. A* **52**, 40 (2016).
135. Z.-Y. Zhu, A. Li, J.-N. Hu, and H. Sagawa, *Phys. Rev. C* **94**, 045803 (2016).
136. J. J. Li, A. Sedrakian, and F. Weber, *Phys. Lett. B* **783**, 234 (2018).